Clean Energy, 2019, Vol. 3, No. 3, 175–201

doi: 10.1093/ce/zkz023
Advance Access Publication Date: 5 October 2019
Homepage: https://academic.oup.com/ce

REVIEW ARTICLE

Reversible solid-oxide cells for clean and sustainable energy

M.B. Mogensen[1,*], M. Chen[1], H.L. Frandsen[1], C. Graves[1], J.B. Hansen[2], K.V. Hansen[1], A. Hauch[1], T. Jacobsen[3], S.H. Jensen[4], T.L. Skafte[1] and X. Sun[1]

[1]Department of Energy Conversion and Storage, Technical University of Denmark (DTU), Frederiksborgvej 399, DK-4000 Roskilde, Denmark
[2]Haldor Topsøe, Haldor Topsøes Allé 1, DK-2800 Lyngby
[3]Department of Chemistry, Technical University of Denmark, DK-2800 Kgs. Lyngby, Denmark
[4]DynElectro ApS, DK-4621 Gadstrup, Denmark

*Corresponding author. E-mail: momo@dtu.dk

Abstract

This review gives first a brief view of the potential availability of sustainable energy. It is clear that over 100 times more solar photovoltaic energy than necessary is readily accessible and that practically available wind alone may deliver sufficient energy supply to the world. Due to the intermittency of these sources, effective and inexpensive energy-conversion and storage technology is needed. Motivation for the possible electrolysis application of reversible solid-oxide cells (RSOCs), including a comparison of power-to-fuel/fuel-to-power to other energy-conversion and storage technologies is presented. RSOC electrochemistry and chemistry of H_2O, CO_2, H_2, CO, C_nH_m (hydrocarbons) and NH_3, including thermodynamics and cell performance, are described. The mechanical strength of popular cell supports is outlined, and newly found stronger materials are mentioned. Common cell-degradation mechanisms, including the effect of common impurities in gases and materials (such as S and Si), plus the deleterious effects of carbon deposition in the fuel electrode are described followed by explanations of how to avoid or ease the consequences. Visions of how RSOCs powered by sustainable energy may be applied on a large scale for the transportation sector via power-to-fuel technology and for integration with the electrical grid together with seasonal storage are presented. Finally, a brief comparison of RSOCs to other electrolysis cells and an outlook with examples of actions necessary to commercialize RSOC applications are sketched.

Keywords: electrolysis; fuel cells; solid-oxide cells; power-to-fuel; electrochemical syngas

Introduction

Global background

A strong demand for clean sustainable energy has appeared in most countries as a result of the fear of the greenhouse effect and the wish for cleaner air. Therefore, the natural question is: is there enough sustainable energy available?

The International Energy Agency (IEA)'s estimate of the World's Total Primary Energy Supply was 13 761 Mtoe (million tons of oil equivalent), corresponding to 18.3 TWy (terawatt years) in 2016. Here, 'supply' means actual supply to customers [1].

The answer is no and yes. Right now, the answer is no, as only a small fraction of sustainable energy is available

Received: 23 April, 2019; **Accepted:** 23 July, 2019

in forms that can cover the energy demand of the world, but, potentially, the answer is yes, because more than enough sustainable energy is available. In order to produce 18.3 TWy electrical energy from photovoltaic cells with conservative 10% efficiency, we need solar irradiation of 183 TW electrical power on average over the year. The average influx of energy from the Sun (corrected for scattering in the atmosphere and absorption by clouds) to the land area between the polar circles corresponds to 21 000 TW average electrical power calculated from data from Tsao et al. [2], i.e. 115 times more than we need. Actually, it takes only a small fraction of the world's deserts to supply all the necessary energy to the world. Fig. 1 shows a global horizontal irradiation (GHI) solar-resource map on which we have shown how limited space it takes even when a photovoltaic (PV) efficiency of 10% is assumed. Table 1 lists the data with 10% efficiency for the six black spots in Fig. 1. It appears that only ~700 000 km^2 is enough, and it only constitutes a relatively small part of each of the six continents' deserts. We note that no use of valuable farmland is necessary for this.

Apart from solar irradiation, energy from the Sun is also manifested in the form of wind and water streams. The potential of these two sources is significantly lower than that of solar radiation. Based on the data from Tsao et al. [2], the realistic technical potential of wind power is 23 TW and of hydropower 1.6 TW electric energy in average. Thus, it seems clear that we will have to rely on solar irradiation as our main sustainable-energy source of the future. Consequently, we need tremendous conversion and storage capacity in order to have a continuous reliable energy supply.

Furthermore, electric power from solar and wind may be generally competitive to fossil fuel within the near future as prices lower than electricity from coal have been reported and the cost seems to continue to drop fast. The global weighted average levelized cost of electricity of utility-scale solar PVs fell by 73% between 2010 and 2017, to USD 0.10/kWh, and large utility-scale PV electricity was down to USD 0.06/kWh in 2017 [4]; trends of further declining prices of PV electricity down to USD 0.03/kWh are claimed. So, solar power is becoming competitive to coal.

The necessity for energy conversion and storage

However, both solar and wind power are intermittent, and thus not always available when needed. Also, the availability of hydropower is not even over the year. Biomass is a sustainable-energy source that is steadily available, but it cannot provide enough energy for the whole world because most of the fertile land area is needed for food production.

Thus, to cover the world's energy demand, it takes efficient and inexpensive energy-conversion and storage systems in order to fully utilize the intermittent solar and wind energy as well as varying hydropower. There are a number of such conversion and storage technologies available, i.e. pumping water into to mountain water reservoirs, in compressed air and batteries. All of these are already in

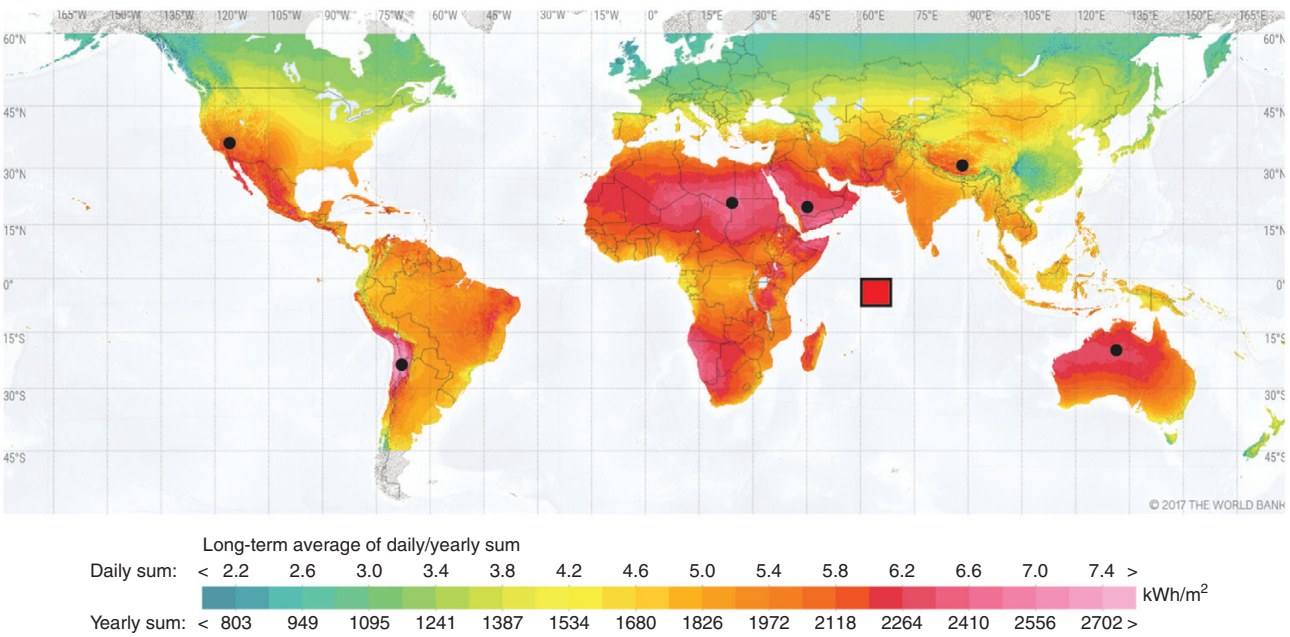

Fig. 1 Global horizontal irradiation (GHI) solar-resource map. The area of PV solar installations necessary to cover today's world energy demand will be <700 000 km^2 in total, if established in e.g. the six areas marked with black spots in desert areas with high GHI over the year. The relatively small size of the total area (700 000 km^2) is visualized as the red square, which is here arbitrarily placed on the map in the Indian Ocean by the equator. Efficiency of the solar installations is assumed to 10%. The map is from solar-resource data obtained from the Global Solar Atlas, owned by the World Bank Group and provided by Solargis [3].

Table 1: Potential solar PV installation area necessary to cover the world energy demand of 18 TWy, based on local horizontal irradiation data for six selected positions shown as black spots in Fig. 1.

Position	GHI year average, kWh m-2	Number of km² needed to produce each 3 TWy per year
Sahara, Libya	2500	105 300
Nevada, USA	2150	122 400
Tibet, China	2150	122 400
Western Australia	2300	114 400
Antofagosta, Chile	2500	105 300
Ar Riyad, Saudi Arabia	2350	112 000
Sum of area of the 6 sites, km²		681 800

use, but none of them is suitable for seasonal storage (over several months to years) and they are not suited for fuelling heavy transport such as trucks, ships and aeroplanes. Thus, fuels like hydrogen, CO_2-neutral carbon-based fuels and/or ammonia produced from sustainable energy are necessary for chemical-energy storage and energy transportation. Conversion technologies that can produce such fuels from sustainable energy will for the time being need electrolysis to convert renewable electrical energy into hydrogen (H_2) from water and carbon monoxide (CO) from carbon dioxide (CO_2). From mixtures of H_2 and CO (syngas), it is possible to produce fuels like methane (CH_4), also called synthetic natural gas (SNG), methanol (CH_3OH), dimethyl ether (CH_3OCH_3, DME) and many other CO_2-neutral fuels based on electrolysis. To this comes ammonia (NH_3). These processes are called power-to-fuel (P2F), power-to-X (P2X) or similar expressions.

The technical advantages of fuels (chemical energy), i.e. P2F or P2X, over e.g. batteries and physical methods may be analysed based on (i) energy density and (ii) equivalent power density.

(i) Table 2 gives approximate numbers for energy density and boiling points (for the chemical-energy carriers). It is clear that, from boiling points and energy-density perspectives, CH_4, DME, CH_3OH and NH_3 are the easiest to handle. The very low boiling point of H_2 adds significant costs in the context of handling it, even though highly compressed H_2 (700 bar) may emerge as an applicable solution in many cases. Compressed air, storage of water at high altitude and batteries do not seem to be an option for storage over long periods in context with the transportation sector. The energy-density argument is in strong favour of conversion by electrolysis into chemical-energy storage.

(ii) The equivalent power density in the transportation of the fuel is also strongly in favour of storage in the form of fuels for aeroplanes, ships and trucks, and also to some extent for passenger cars. The following short example illustrates this. Assuming a filling rate of 20 L/min for liquid DME means that it takes 3 min to get 60 L = 1320 MJ on board. This is equivalent to 7.3 MW of power. For comparison: Li-batteries require something like 8 h to get recharged without unnecessary damage to the battery life. For a 300-kg battery package (1 MJ/kg), it takes 8 h to get 300 MJ on board. This is a power of ~10 kW, or more than 700 times slower than filling DME. Faster charging is possible today, and a power of up to 350 kW has been reported. In this case, the charging rate is only 20 times slower and the effect of this rate on battery lifetime is unclear. We think that this power argument is still a strong argument in favour of P2F.

Table 2 Data for comparison of volumetric and gravimetric energy density for selected energy-storage technologies. Values are only approximate because of scatter in literature data. All handling technologies are well tested and seem safe.

Storage type	MJ/L	MJ/kg	Boiling point, °C
Liquid methane	22	56	–162
Liquid dimethyl ether (DME)	22	30	–25
Methanol	16	20	+65
Liquid ammonia	12	19	–33
Liquid hydrogen	10	141	–253
Compressed air—20 MPa	0.1	0.4	
Water at 100 m elevation	10^{-3}	10^{-3}	
Lead acid batteries	0.4	0.15	
Li-ion batteries	2	1	

The reversible solid-oxide cell (RSOC) as a potent energy converter

The RSOC is very potent technology for these purposes, but it has to reach a more mature state (lower cost, longer lifetime, improved reliability) before it is ready for the general power and fuel market. Therefore, more RSOC research and development (R&D) has to be carried out. The present paper is a brief review and a guide to solid-oxide electrolysis cell (SOEC) and solid-oxide fuel cell (SOFC) literature, mainly about the cells based on: gaseous fuel|Ni–YSZ|YSZ|LSTr-YSZ|air or O_2; here, YSZ means yttria stabilized zirconia. Here, LSTr means $(La_{1-x}Sr_x)_sTrO_3$, $0.5 < x < 1$ and $0.9 < s < 1$, Tr is one or more of the first row of transition metals of the periodic table. Below, in the 'New types of RSOC' section, is given a brief description of alternative RSOCs without high amounts of Ni, and of RSOC competitors in the form of cells with low-temperature proton-conducting electrolytes and alkaline electrolytes. This comparison shows that RSOCs hold the highest potential in terms of efficiency and potentially low-cost materials. Further, reversibility in order to convert sustainable electricity into chemical energy and back again into electricity is only possessed using RSOCs.

Naturally, it is not possible to cover all solid-oxide cell (SOC) literature, because a search using SciFinder on 'solid oxide fuel cell' and 'solid oxide electrolysis cell' returns

over 37 000 and 15 000 references, respectively. Google Scholar searches give millions of hits for both. Thus, the references in the present paper are just selected books and articles that we know and have found essential. The present description on motivation for SOC R&D and on cell performance and durability is based on own experience and on SOFC books plus many SOC reviews such as references [5–10].

1 RSOC principle, materials and thermodynamics

An RSOC may be operated either as an SOFC or as an SOEC. This means that the very same cell can interchangeably be used in both modes. The overall principle is sketched in Fig. 2.

1.1 Cell design and materials

Fig. 3 shows an artificially coloured scanning electron microscope (SEM) micrograph of a cell of the same popular design as in Fig. 2—the so-called fuel-electrode-supported flat-plate design. The cell support and the fuel electrode are both made of nickel–yttria stabilized zirconia (Ni–YSZ cermet). The mechanical support is usually called 'the fuel electrode support', because it is made of approximately the same Ni–YSZ material as the fuel electrode. The support is typically made of a composite of 40 vol% Ni and 60 vol% $Zr_{0.94}Y_{0.06}O_{1.96}$ with a relatively coarse structure with 30–35% porosity. The active fuel electrode is made of a Ni and $Zr_{0.84}Y_{0.16}O_{1.92}$ composite with the same 40 vol%/60vol%, but with a significantly finer structure and a lower porosity than the cell support. $Zr_{0.94}Y_{0.06}O_{1.96}$ is usually denoted as 3YSZ and $Zr_{084}Y_{0.16}O_{1.92}$ as 8YSZ, because they contain approximately 3 and 8 mol% Y_2O_3, respectively. The full cell support is about 350 μm thick [11].

Both Ni–YSZ cermet layers are prepared and sintered as NiO–YSZ composites and then the NiO is reduced to metallic Ni when exposed to H_2 or polarized to e.g. –1 V versus an O_2 reference electrode (1 bar, 1000°C) for 1 h for $(La_{0.75}Sr_{0.25})_{0.95}MnO_3$ (LSM) and $(La_{0.6}Sr_{0.4})_{0.98}Co_{0.2}Fe0_{.8}O_{3-\delta}$ (LSCF) [11] and thereafter the temperature is reduced to the operation temperature. For LSC cells, the NiO reduction temperature is 850°C and the hold time is 2 h. The lower the NiO reduction temperature, the longer the necessary hold time [11].

The electrolyte consists of 8YSZ, as this composition has the highest oxide ion conductivity of yttria-doped zirconia. Ten mol% scandia (Sc_2O_3)-doped zirconia has even higher ion conductivity, but is more expensive [12]. The high conductivity is also the reason for using 8YSZ in the active fuel electrode. Several other SOC electrolyte materials exist, but all are less mechanically strong and less thermodynamically stable [12, 13]. The reason for using 3YSZ in the support is that this is one of the mechanically strongest ceramics due to its martensitic transformation ability (see more below).

For the time being, one of the most popular oxygen-electrode materials are the perovskite-structured $(La_{0.6}Sr_{0.4})_{0.98}CoO_3$ (LSC) and LSCF, of which both are excellent oxygen-reduction and oxide-ion-oxidation catalysts [14]. Furthermore, LSC is a mixed-oxide ion and electron conductor at 750°C and above. However, LSC reacts with YSZ at sintering temperature, and therefore a reaction barrier of $Ce_{0.9}Gd_{0.1}O_{1.95}$ (CGO) is placed between the YSZ electrolyte and the perovskite, and the composite electrode is LSC mixed with CGO. Other Ruddlesden-Popper-structured oxides of the type Ln_2MtO_4, where Ln is a trivalent big lanthanide metal ion and Mt is a small divalent transition metal ion, have been reported as good O_2-electrode materials (see e.g. [15, 16]).

The area of a flat-plate single cell is typically in the range of 80–150 cm^2.

Many other designs and other cell materials and compositions have been reported. For some decades, oxygen electrodes of $(La_{1-x}Sr_x)_sMnO_3$ (LSM) were preferred due the

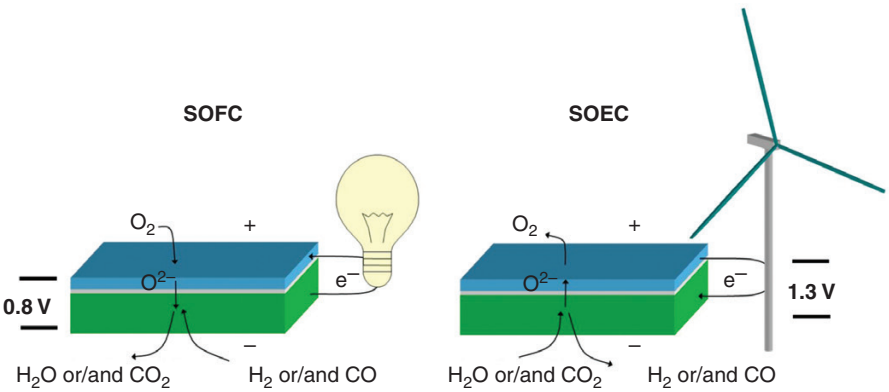

Fig. 2 Sketch of the principle of SOCs in SOFC and SOEC modes of operation. The blue top layer illustrates the porous oxygen electrode, the white layer is the dense oxide ion-conducting electrolyte and the green layer is the porous-fuel electrode plus the porous structural support of the cell. The operation temperature is typically around 750–800°C. The open-circuit voltage (OCV) of an SOC with 50% H_2O + 50% H_2 at the fuel electrode and pure oxygen at the oxygen electrode, 1 bar and 750°C is close to 1.0 V.

high thermodynamic stability of LSM, and perhaps the stability issue may still convince some RSOC developers that this is the best oxygen-electrode material for RSOCs.

1.2 Cell stacks

In practice, single flat-plate cells are put into series in stacks or assemblies. A stack typically consists of 50–100 cells in order to obtain applicable voltages. Fig. 4 shows an expanded sketch of a bipolar flat-plate cell stack. A full stack must also contain gas seals and manifolds of some kind [7]. The dense electrolyte layer, the dense interconnector plate and the seals prevent the mixing of fuel gas and oxidant gas (oxygen or air).

Apart from this, a large number of other stack designs have been proposed and tested, such as round tubular, flat tubular and transverse stripe tubular cell arrangements, just to mention a few [17].

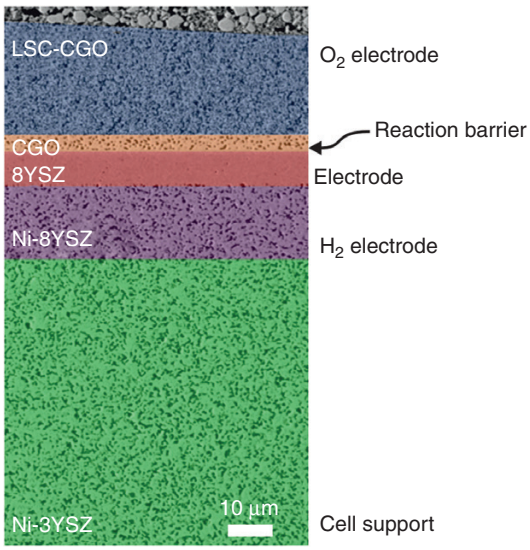

Fig. 3 Artificially coloured scanning electron microscope (SEM) micrograph of cross-section of a DTU-manufactured solid-oxide cell. Only the section of active cell parts and a minor part of the cell support are shown, with dimensions in accordance with the scale bar in the figure. The full cell support is about 350 µm thick.

1.3 RSOC thermodynamics

Figs 5 and 6 show reversible thermodynamic diagrams for H_2O and CO_2 electrolysis at atmospheric pressure. If the reactions ($½\ O_2 + H_2 \rightarrow H_2O$ and $½\ O_2 + CO \rightarrow CO_2$) are reversed in the top of the figures, and 'demand' is exchanged for 'content', then exactly the same figures give the thermodynamics for the H_2 and CO fuel cells [9]. The relation between the two *y*-axes is simply the fact that energy measured in the unit of 'volt (V)' is equal to the energy measured in the unit of 'kJ/mol' divided by 2F (F is Faradays number). We may see the following in Figs 5 and 6.

At standard pressure (1 bar) and if partial pressures of $pH_2/pH_2O = 1$ and $pO_2 = 1$ bar, then $E_{eq} = \Delta G_f/2F$, where E_{eq} is the equilibrium voltage of an electrolysis cell or fuel cell of any kind and ΔG_f is Gibbs free energy of the formation of H_2O at the given temperature. The equivalent relations are valid for the CO_2–CO cell.

That $\Delta H_f/\Delta G_f > 1$, where ΔH_f is the enthalpy of formation, means that the electrolysis process is endothermic and the fuel-cell process is exothermic. Thus, in electrolysis mode, when the applied cell voltage E_{cell} is equal to $E_{tn} = \Delta H_f/2F$, then there is no heat production from the cell, i.e. the cell polarization, $\Delta E_{pol} = E_{tn} - E_{eq} = \Delta H_f/2F - \Delta G_f/2F$. In other words, E_{tn} is the thermoneutral voltage. The gap between the green and black curves in both Figs 5 and 6 means that the electrical-energy efficiency, $\eta_{el} = 100\%$ at $E_{cell} = E_{tn}$ (in the case of no heat loss to the surroundings)

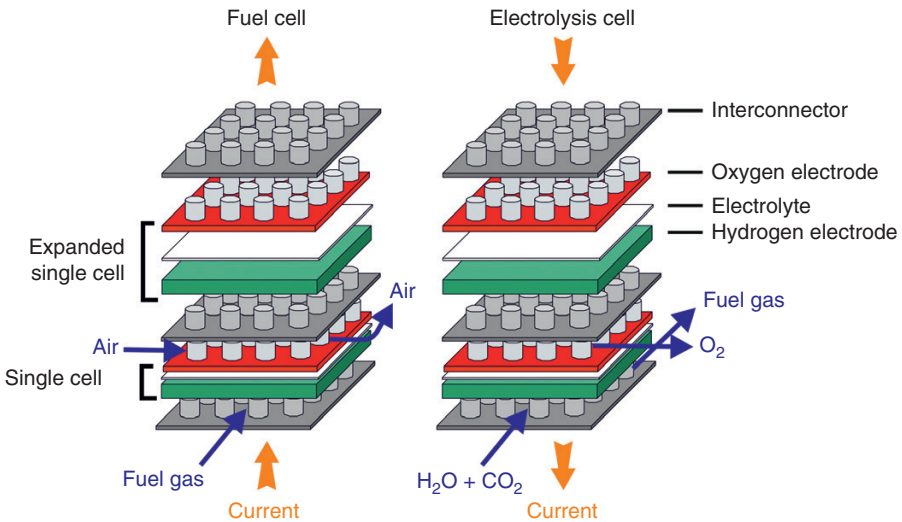

Fig. 4 Sketch of the inside of a solid-oxide cell stack operated in fuel-cell mode (left) and electrolysis-cell mode (right). The flow-field cylinders are regarded as an ideal design, but so far not realized in practical manufacturing. The interconnect is often a thin plate or other structure made of ferritic stainless steel [17].

and that, in the interval of $E_{eq} < E_{cell} < E_{tn}$, it is necessary to supply heat in order to keep the cell temperature.

The electrical-energy efficiency is higher than 100% under such conditions but, naturally, the total energy will never reach 100%, as, in such cases, a heat supply is necessary to compensate for the endothermic heat demand plus the heat loss to the surroundings. Fig. 5 reveals that relatively low-grade heat having a temperature a little above 100°C is able to supply the necessary heat for evaporation of liquid H_2O. This may be advantageous in cases where SOECs are integrated with other industrial processes that produce heat.

The current–voltage (iV) curve is approximately linear for RSOCs, i.e. $i \propto E_{cell} - E_{eq}$, the cell polarization. Everything else being equal, the price of H_2 and CO produced by electrolysis will be inversely proportional to the current density, i. In many cases, it is advantageous to operate in SOEC mode at a cell voltage just above E_{tn} because then no cooling or heating system for stacks is necessary. (The slightly higher voltage than E_{tn} is necessary in order to deliver the heat loss to the surroundings.) So, Figs 5 and 6 indicate that the cheapest gas will be produced at the highest possible temperature. The advantage of high temperature is further supported by the fact that polarization resistance is lower the higher the temperature is. However, everything is not equal with increasing temperature, as the stability of stack materials decreases rapidly with increasing temperature, and thus the optimal conditions have to be found as a compromise.

Anyway, the facts above about SOECs and the fact that most other electrolysis-cell types are not reversible mean that the RSOC is significantly more efficient and more flexible in operation than conversion, storage and re-conversion systems based on lower-temperature electrolysis and fuel cells.

2 Status of RSOC technology

This chapter reviews the status of SOC technology with respect to performance, durability and mechanical strength, including area-specific resistance (ASR), power density, degradation types and rates for various types of RSOCs, all in relation to cell materials, design and operation conditions including sensitivity to impurities.

2.1 RSOC electrochemistry and performance

As mentioned above, it is important that an RSOC stack in SOEC mode be run as close to the thermoneutral condition as possible. E_{tn} is in the range of 1.3–1.5 V for the co-electrolysis of CO_2 and H_2O in one gas mixture. The exact value depends on the operating conditions, including the composition of the CO_2 or H_2O feed with a low concentration of CO or H_2, or a mix of all of them [18]. Figs 5 and 6 also reveal that there is no possibility of avoiding a lot of heat release in SOFC mode using H_2 and CO as fuel. Using e.g. CH_4 plus H_2O as fuel in SOFC mode (internal reforming) can limit the heat production significantly. The production of syngas with the right composition and high pressure (about 30 bar) using SOECs may produce CH_4 inside the fuel-electrode compartment [19] but, in order to make this version of the RSOC technology commercial, it is necessary to decrease the area-specific internal cell resistance to about 0.4 Ω cm^{-2} at 450°C in order to be able to run the cell at –1 A cm^{-2} at a cell polarization of 0.4 V, i.e. a cell voltage of 1.4 V. This is close to the thermoneutral potential of a 50%/50% mixture of H_2O/CO_2. However, it will require significant further development of the RSOC to lower the internal cell resistance sufficiently to make this possible, but there is no fundamental reason why it should not be possible. Until this has happened, we will have to

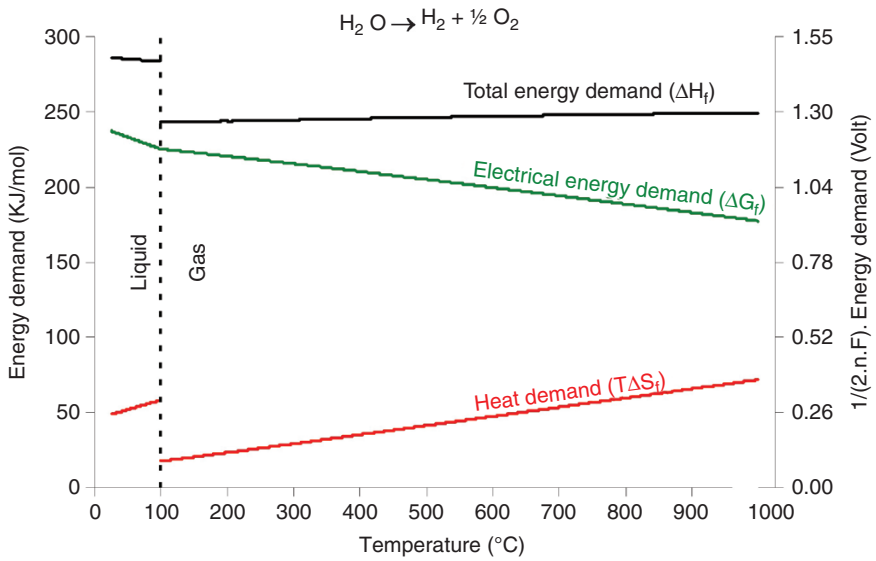

Fig. 5 Reversible thermodynamics for H_2O electrolysis at atmospheric pressure. If the reaction is reversed (½ O_2 + H_2 → H_2O) in the top of the figure, and 'demand' is exchanged for 'content', then exactly the same figure gives the thermodynamics for the H_2 fuel cell. Reprinted from [9] with permission from American Chemical Society.

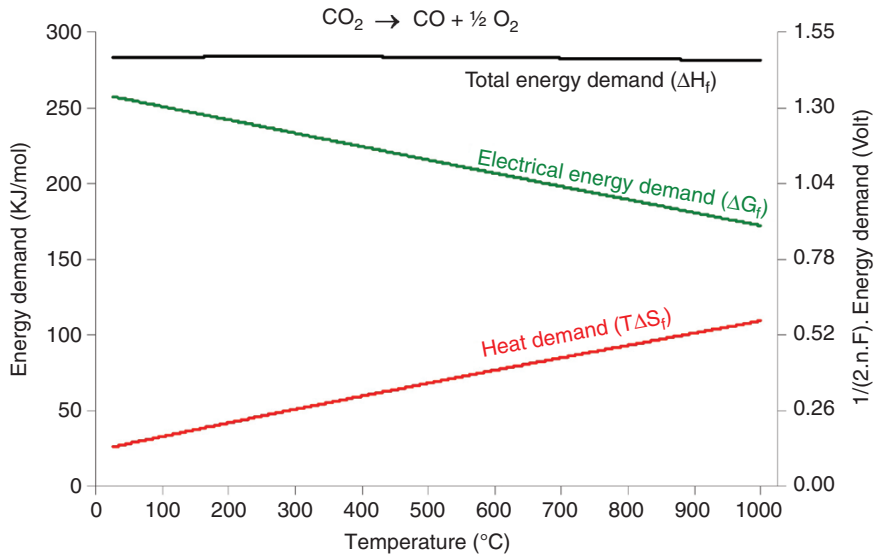

Fig. 6 Thermodynamics of CO_2 electrolysis at atmospheric pressure. If the reaction is reversed (½ O_2 + CO → CO_2) in the top of the figure, and 'demand' is exchanged for 'content', then exactly the same figure gives the thermodynamics for the CO fuel cell. Reprinted from [9] with permission from American Chemical Society.

make our CH_4 by taking the syngas from the electrolyser to a catalytic methanation reactor at 30 bar and 400°C, or to other types of catalytic reactors that can produce synthetic fuels (synfuels) of almost any kind. Such reactors are already commercially available in the chemical industry.

Another chemistry that may be used in the future for chemical storage is based on ammonia (NH_3). The role of RSOC electrochemistry in this context is to produce H_2 in SOEC mode and then react some of the H_2 with all O_2 of the air to make pure nitrogen (N_2) using sustainable electricity [20]. Then, this N_2 is mixed with H_2 and reacted to NH_3 in a Haber-Bosch process [21]. When electricity again is needed, this can be produced using an RSOC in SOFC mode, which is fed with NH_3, as this is a fine fuel for SOFCs [22].

Furthermore, NH_3 is already the most produced chemical in the world, with a yearly tonnage above 10^8 tons [23] based on fossil fuels. NH_3 is used as a fertilizer. The possibility of supplying H_2 produced by electrolysis to produce NH_3 can avoid the use of large quantities of natural gas and thus significantly lower the release of CO_2 into the atmosphere in the order of 1% of the total release of CO_2 to the atmosphere by humans [24].

Finally, there is the vast area of hydrocarbons and oxyhydrocarbons as synthetic CO_2-neutral fuels and as fuels for SOFCs. This is mainly chemistry rather than electrochemistry for the time being, as the RSOC temperature (>750°C) is too high for these carbon-based fuels, which are so brilliant for the storage of energy (see Table 2). Below, the hydrocarbon issues will be briefly described.

2.2 Reversibility and fuel chemistry

2.2.1 *H_2O/H_2 and CO_2/CO*

The electrochemical reactions for the various electrode reactions in RSOC cells are given as follows.

The oxygen electrode is in all cases the positive electrode and the reaction is

$$O^{2-} \rightleftharpoons {}^{1}/_{2}\, O_2 + 2e^- \quad (1)$$

The reaction towards the right is oxygen evolution (electrolysis mode) and to towards the left is oxygen reduction (fuel-cell mode).

The fuel electrode is in all cases the negative electrode and, for H_2O/H_2, the reaction is

$$H_2O + 2e^- \rightleftharpoons H_2 + O^{2-} \quad (2)$$

Again, towards the right is hydrogen evolution (electrolysis mode) and towards the left is hydrogen oxidation (fuel-cell mode).

In analogy, the fuel-electrode reaction for CO_2/CO is

$$CO_2 + 2e^{2-} \rightleftharpoons CO + O^{2-} \quad (3)$$

The total reactions ($H_2O \rightleftharpoons H_2 + ½O_2$ and $CO_2 \rightleftharpoons CO + ½O_2$) change in both cases the number of gas molecules from 1 to 1½ and, as gas contains a lot of entropy, this is the reason for the strong endothermic electrolysis and exothermic fuel-cell reactions as visualized in Figs 5 and 6.

Fig. 7 shows three iV-curves for three SOCs with different compositions of oxygen electrodes, all produced and tested at the Department of Energy Conversion and Storage, DTU. At OCV, the Ni–YSZ|YSZ|LSM-YSZ SOC shows a low performance (0.27 Ω cm²) compared with Ni–YSZ|YSZ|CGO|LSCF-CGO (0.19 Ω cm²) and Ni–YSZ|YSZ|CGO|LSC-CGO (0.15 Ω cm²) [8]. All three cell types show good reversibility in the sense that the iV-curves pass back and forth over zero current density in a linear and symmetrical manner, i.e. the slopes (polarization resistances) are the same on both sides of the zero current.

Similar reversible behaviour has been reported for the electrolysis of CO_2 and for the co-electrolysis of mixtures of H_2O and CO_2 [9].

Initial performance and durability of RSOCs look fine in the reported literature. Figs 8–11 show the best reported data that we know of [25, 26]. These tests of cells from FuelCell Energy are indeed impressive. However, when comparing literature data, we have to be aware of the circumstances of the test. An example is that, if we compare the DTU cell test with the LSC electrode in Fig. 7 and the 800°C test of Fig. 8, there is a great difference even though they are both tested at 800°C. However, ASRs measured as the slope of the almost linear part of the curve from 0 to 0. 5 A cm^{-2} are both close to 0.15 Ω cm^{-2}. A main difference is that the DTU cell is tested with a 50/50 ratio of pH_2/pH_2O to the fuel electrode and pure O_2 to the oxygen electrode in order to simulate the average conditions of a practical SOEC, whereas the test at FuelCell Energy is tested with ~2/98 ratio of pH_2/pH_2O to the fuel electrode and air to the oxygen electrode, possibly with the purpose of obtaining the maximum hydrogen-production rate. A consequence of the differences in the gases supplied to the electrodes is that there is about 0.2 V difference in OCV between the tests. No details about the cell of Fig. 8 are presented in [25], but Dr Wood informed us at the conference that the cell was made of classic SOC materials. Thus, the two cells should be comparable and, in spite of the huge difference in their immediate appearance, they are in fact quite similar when the results are compared in comparable details.

It is also noticeable that the durability in SOFC mode looks as if it is considerably better than in SOEC mode. This is probably the case for most cells and cell tests done galvanostatically in SOEC mode seem to be degrading slightly faster (and earlier than a couple of years ago: much faster). One reason may be that the two operation modes have different sensitivities to common impurities (see below).

Fig. 12 illustrates a small laboratory demonstration that an existing Haldor Topsøe A/S (HTAS) RSOC stack is able to load-follow in a real energy system. It shows 16 days (384 h) of a test that ran for approximately 1600 h in total, of which about 1200 h were for the reversible wind-load-balancing profile. The stack was an eight-cell HTAS Delta-type stack. The profile was generated directly from time-series data of wind-power supply and electricity demand from the Danish island of Ærø. The stack managed to operate in these highly variable conditions of complete load-balancing that are needed in order to enable 100% renewable energy for the region. The stack performance was not harmed by these interruptions, demonstrating stable performance for several hundred hours [27].

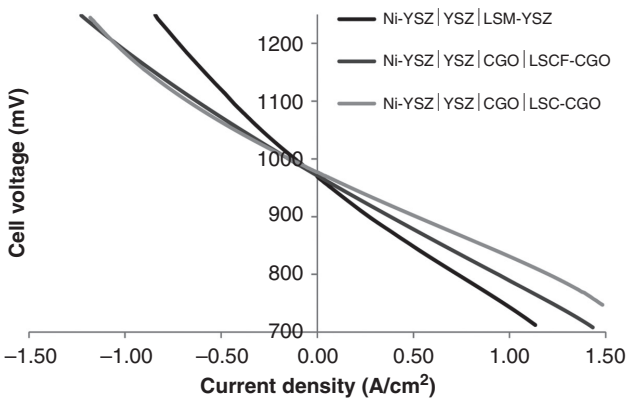

Fig. 7 iV-curves for three planar Ni–YSZ-based cells of the types illustrated in Fig. 3: Ni–YSZ|YSZ|LSM-YSZ, Ni–YSZ|YSZ|CGObarrier|LSCF-CGO and Ni–YSZ|YSZ|CGO|LSC-CGO. Operating conditions: 800°C, 50% H_2O–50% H_2 was supplied to the fuel electrode and O_2 to the oxygen electrode. Reprinted from [9] with permission from American Chemical Society.

2.2.2 *CxHyOz*

Hydrocarbon and oxyhydrocarbon ($C_xH_yO_z$) cannot yet in general be used as direct fuels in Ni–YSZ-based SOFCs

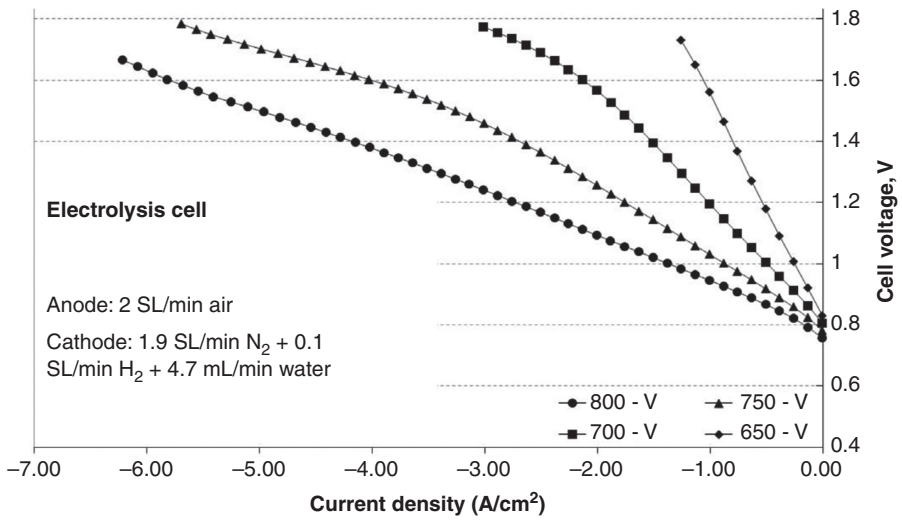

Fig. 8 Voltage versus current density of an SOEC single cell (stack repeating unit) from FuelCell Energy, test temperature 650–800°C. After Wood et al. [25] with permission from European Fuel Cell Forum AG.

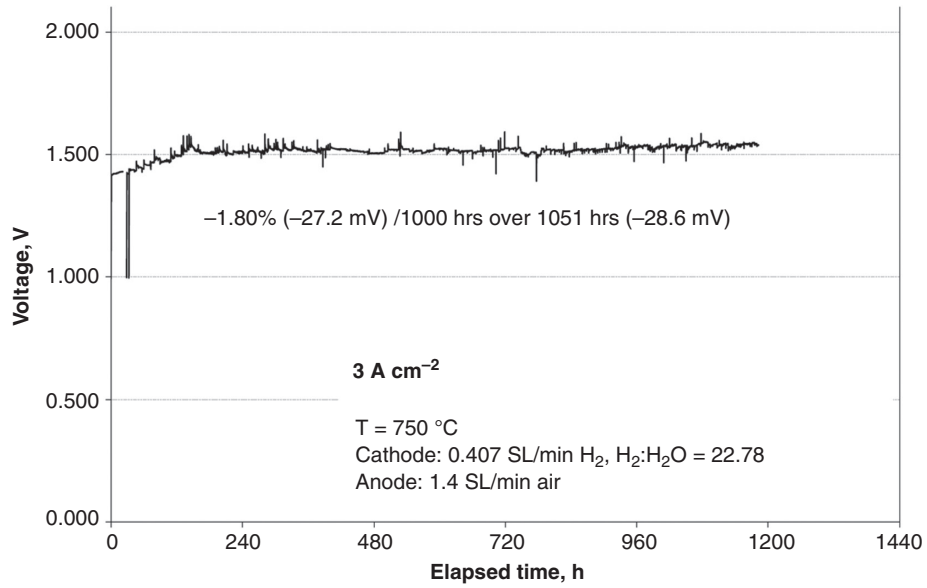

Fig. 9 Cell voltage as a function of time for an SOEC from FuelCell Energy. After Wood et al. [25] with permission from European Fuel Cell Forum AG.

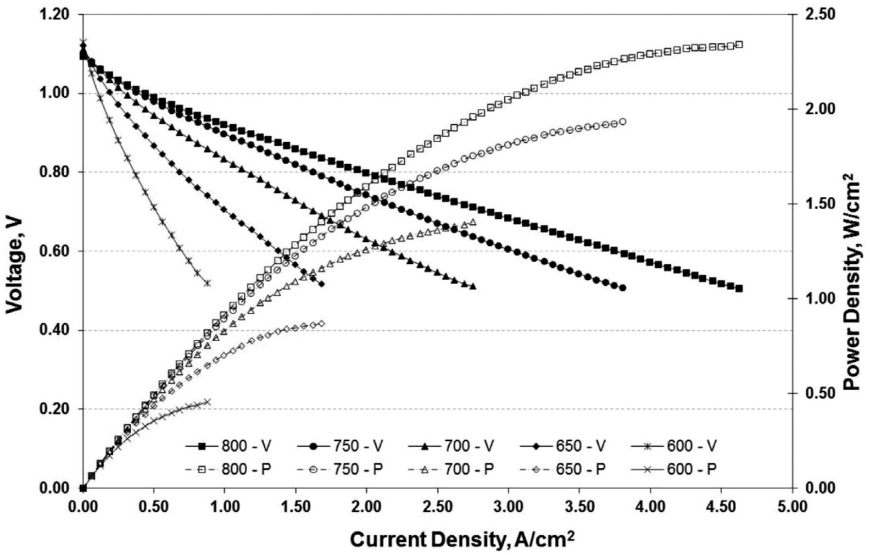

Fig. 10 Initial voltage and power density as functions of current density of a single-stack repeat unit, at 600–800°C. From FuelCell Energy. After Borglum & Ghezel-Ayagh [26] with permission from European Fuel Cell Forum AG.

because they will crack, carbon will precipitate and the fuel electrode will become blocked and destroyed by the carbon (see the 'Carbon deposition in Ni–YSZ SOC electrodes' section below). However, carbon-containing fuels can be used after catalytic treatment of the fuels [28–30]. Hydrocarbons may be reformed externally into H_2 and CO. Natural gas may also be reformed internally, as Ni is the reforming catalyst in all three cases below, and the Ni–YSZ cermet support and fuel electrodes of RSOCs are fine practical Ni-catalysts.

The most-used reforming method is steam reforming, which follows the chemical reaction

$$C_nH_m + n\ H_2O \rightarrow n\ CO + (n + m/2)\ H_2 \quad (4)$$

and the water–gas shift reaction (Equation (5)) always run in parallel with Equation (4):

$$CO + H_2O \rightleftharpoons CO_2 + H_2 \quad (5)$$

Another important reaction is the methanation reaction:

$$CO + 3H_2 \rightleftharpoons CH_4 + H_2O \quad (6)$$

and Equation (6) is reversible, but it is totally shifted to the left under the RSOC-operating conditions of today, i.e. temperatures of 700°C and above, and atmospheric pressure. It is necessary to decrease the temperature to <500°C and pressurize to about 30 bar in order to shift it sufficiently to the right.

Steam reforming is a strongly endothermic reaction that needs a lot of heat and will cool the inlet of the fuel

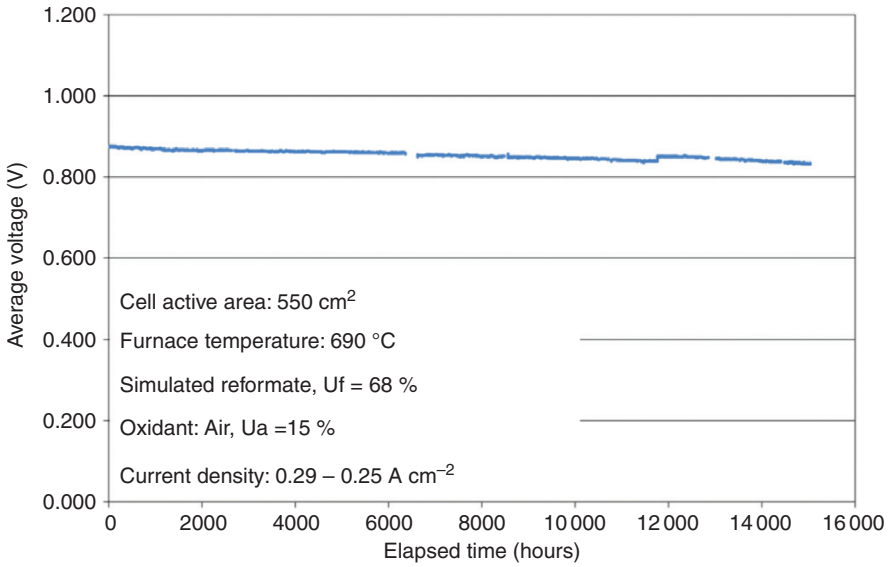

Fig. 11 Average cell voltage versus time for a 64 SOFC stack, 25 × 25 cm^2, cells from FuelCell Energy. After Borglum & Ghezel-Ayagh [26] with permission from European Fuel Cell Forum AG.

electrode in the case of internal reforming. Thus, this puts serious demands on the mechanical strength of the cell and stack, but SOC technology has been developed to withstand this; however, when the stack can tolerate the cooling by internal-reforming cooling, it is advantageous, as it helps in cooling the very exothermic H_2 and CO oxidation processes in an SOFC. Thereby, the amount of surplus airflow can be decreased and less energy is lost to drive the high airflow that is usually used for cooling the SOFC stack [29]. Interestingly, this opens the possibility for an efficient way of using easily cracked fuels like ethanol or diesel, which cannot be used directly because of the mentioned carbon deposition in the Ni–YSZ electrode by the cracking process. Such fuel can be catalytically converted into a mixture of mainly CH_4 and H_2. Using this as the fuel will help in cooling the stack [29]. Control of the reforming reaction rate may be accomplished by having a tiny concentration of sulphur compounds in the gas feed, as this will impede the reforming rate [29].

2.2.3 *NH_3 as an alternative carbon-free fuel*

In the case of NH_3 as the fuel for an RSOC in fuel-cell mode, it works exactly as if the fuel was a mixture of H_2/N_2 = 3/1 [22] (see Fig. 13). Furthermore, fairly low degradation rates have been demonstrated on cells and stacks [30]. NH_3 cracking seems to be the first step in the conversion of the NH_3 in the fuel electrode, and it seems to take a lot of Ni surface to fully catalyse the cracking process at temperatures of 700°C and below [30].

The synthesis of NH_3 in an SOEC is not possible, as the equilibrium reaction

$$3\,H_2 + N_2 \rightleftharpoons 3NH_3 \qquad (7)$$

is totally shifted to the left at temperatures above 600°C. This means that the synthesis of sustainable NH_3 has to be done by producing H_2 by H_2O electrolysis and by producing N_2 from air by the conversion of O_2 with H_2 followed by condensation of the formed H_2O.

2.3 Performance and durability considerations

A general rule of thumb seems to be that the better the initial performance, the more durable the cell or stack will be with respect to electrochemical degradation. This observation probably relies on the fact that the cell polarization is the driving force for the cell processes and, in most cases, also drives the degradation, while the tests are usually carried out in galvanostatic mode (constant current density), as this is the most easily seen from an instrumental point of view. However, it might be helpful for our understanding of degradation processes to do more tests in potentiostatic mode (constant potential), because galvanostatic mode will increase the overvoltage of the electrode process as the degradation processes proceed. Thus, galvanostatic testing may be a kind of uncontrolled accelerated testing. In spite of this, it is not guaranteed that the durability always will be better in potentiostatic than in galvanostatic tests, but it will probably be different [31].

Recent reviews on general degradation mechanisms and measures to prevent and repair degradation have been published by Graves [32] and Skafte [33]. These works are in particular relevant to bipolar flat-plate stacks with Ni–YSZ-supported cells (see Figs 4 and 14). The RSOC bipolar flat-plate stack must be able to convert the reactant gases, CO_2 and/or H_2O, and electrical energy into CO and/or H_2 in SOEC mode, and the reverse in SOFC mode. This takes a number of specific functions, which may be carried out by the following components in a stack repeating unit (SRU): (i) an electrochemical cell, (ii) a combined mechanical cell support and current distributor, (iii) an electric interconnector, which separates the reactant gases of two

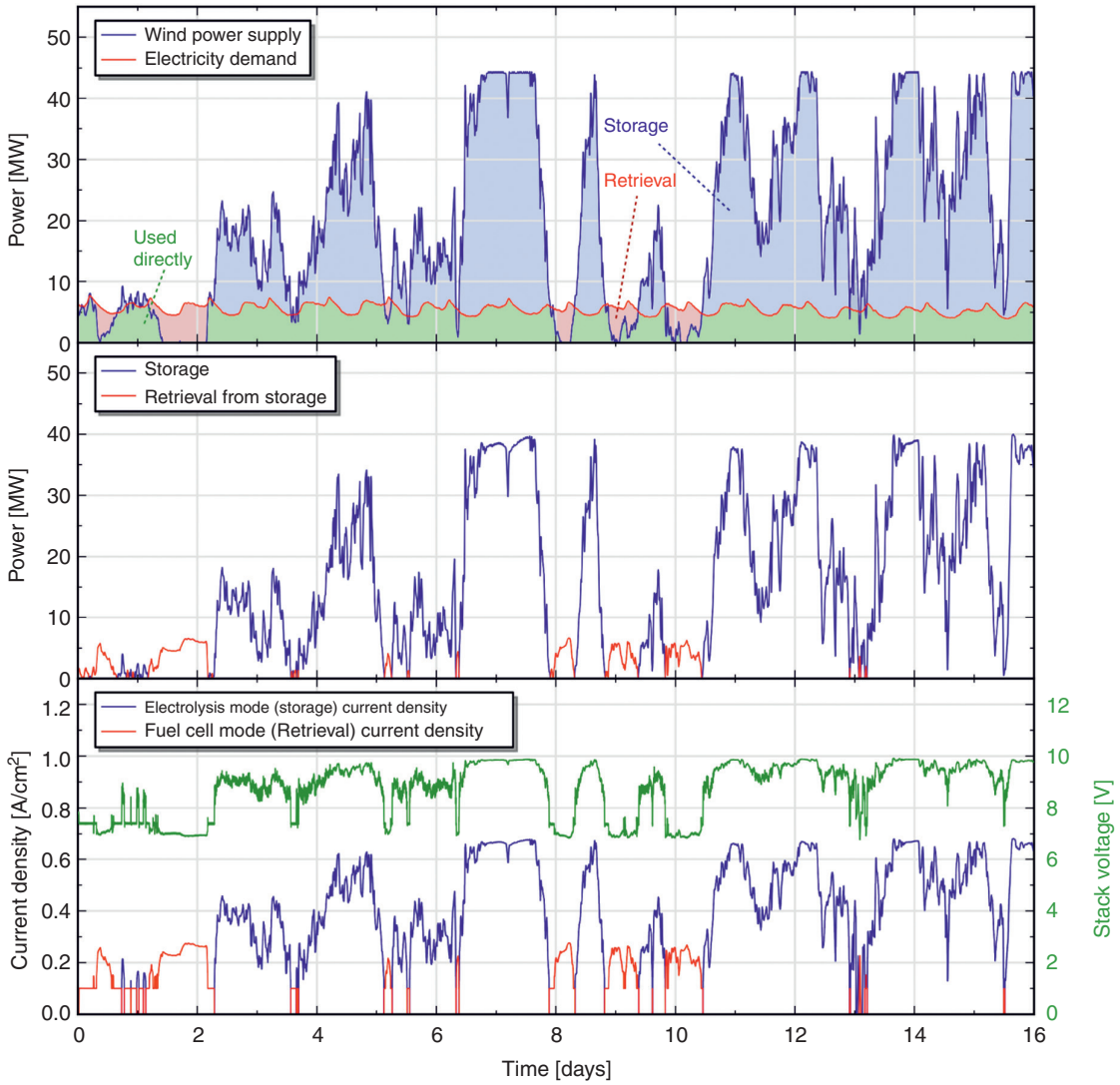

Fig. 12 Illustration of the RSOC '100% wind power' energy-balancing profile and stack-test data. In the top plot, the time-series wind-power-supply and electricity-demand data (2010) for Ærø island in Denmark are shown. The shaded regions indicate where the energy would be used directly, stored and retrieved from storage. The middle plot shows the result of the energy-balancing simulation. The bottom plot shows the data from the stack test that was operated according to the energy-balancing profile defined by the simulation [27].

cells, (iv) two gas collectors (SOECs)/distributors (SOFCs)—one for the fuel and one for the oxygen, (v) electrode edge seals and (vi) two end plates. The cell consists of an air electrode, electrolyte and fuel electrode on top of a support, as shown in Fig. 14 [34].

First of all, the thermodynamic and mechanical stability of all the components on the fuel side (YSZ, Ni–YSZ, glass seals) in contact with reactants (H_2, H_2O, CO, CO_2) and on the oxidant side (YSZ, YSZ-LSM, glass seals) in contact with O_2 and N_2 is important. In general, a solid material is not mechanically stable if it has a geometric flaw (e.g. a notch at the surface) and the stress state is high enough to overcome the necessary free energy of the formation of the surface(s) of the material(s). Further, the material will react if ($\Delta G_{reaction}$ + electrical gain in energy) is negative and a reaction mechanism exists through which the reaction can take place. Actually, the electrical potential of the materials may influence also the mechanical stability, because the precise composition of materials is dependent on the potential and the mechanical properties are dependent on the composition of the material. $\Delta G_{formation}$ = –975 kJ/mol ZrO_2 at 800°C, which translates into a theoretical electrochemical potential stability range of ~2.5 V, which is the maximum stability interval for a zirconia-based electrolyte, i.e. if the potential of the cathode (negative SOEC electrode) is lower than –2.5 V versus an oxygen reference electrode (1 bar, 800°C), then the YSZ will split into Zr metal and O_2 gas. In practice, the stability interval may be significantly lower than 2.5 V, because YSZ will start changing composition at less negative potentials than –2.5 V versus O_2 (1 bar) if it can react with other cell components [35, 36].

2.3.1 *Mechanical strength of the Ni–YSZ support*

While strong and ductile metal-supported cells are being developed [37, 38], the majority of current cell designs rely on zirconia as the structural component, either as a Ni–YSZ support or as the electrolyte as a support. The three most commonly used materials are 8YSZ or 10Sc1CeSZ (or 10Sc1YSZ) for electrolytes with high ionic conductivity and in the Ni–YSZ support 3YSZ with superior strength, which stems from the martensitic phase transformation from tetragonal to monoclinic zirconia occurring at crack tips. It hinders the crack from growing and effectively enhances the strength [39]. While this is a well-proven mechanism at room temperature, the use of this material may have some drawbacks at higher temperatures [40], as we will cover in the following.

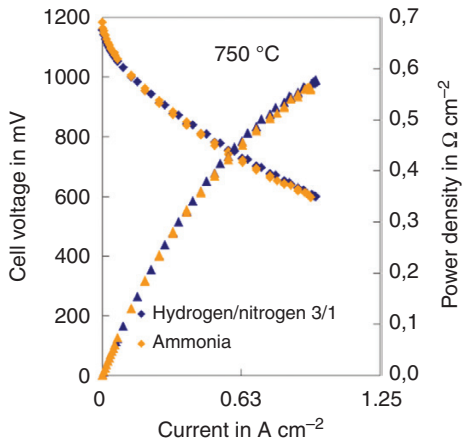

Fig. 13 Cell-voltage and power-density curves for a Ni–YSZ|YSZ|LSM-YSZ fed with ammonia (yellow triangles) and H_2/N_2 = 3/1 (blue triangles) [22].

The strength has been shown to strongly depend on the temperature in the reduced condition when Ni–3YSZ is used as an electrode support [41]. This is primarily believed to be due to the strong temperature dependency of the energy dissipation of the plastically deforming nickel phase and not so much the 3YSZ. In the oxidized condition, i.e. as NiO–3YSZ, the strength is almost independent of temperature [41]. In NiO–3YSZ, the 3YSZ phase is the stronger and thus strength-determining. The strength increase from the phase transformation of 3YSZ is expected to vanish as the temperature gets beyond the metastable regime, where the phase transformation will occur [39]. Yet, 3YSZ is tougher than 8YSZ at high temperatures [40]. One hypothesis of the temperature independency is that the 3YSZ phase is shielded by compressive residual stresses in the microstructure (when cooled from sintering due to the higher thermal-expansion coefficient (TEC = 14 ·10^{-6} K^{-1}) of NiO compared to 3YSZ (TEC = 11· 10^{-6} K^{-1})). More recent research indicates that it is the slow grain growth in 3YSZ through sintering and resulting small grains as compared to 8YSZ that are partially the reason that 3YSZ maintains its strength [40].

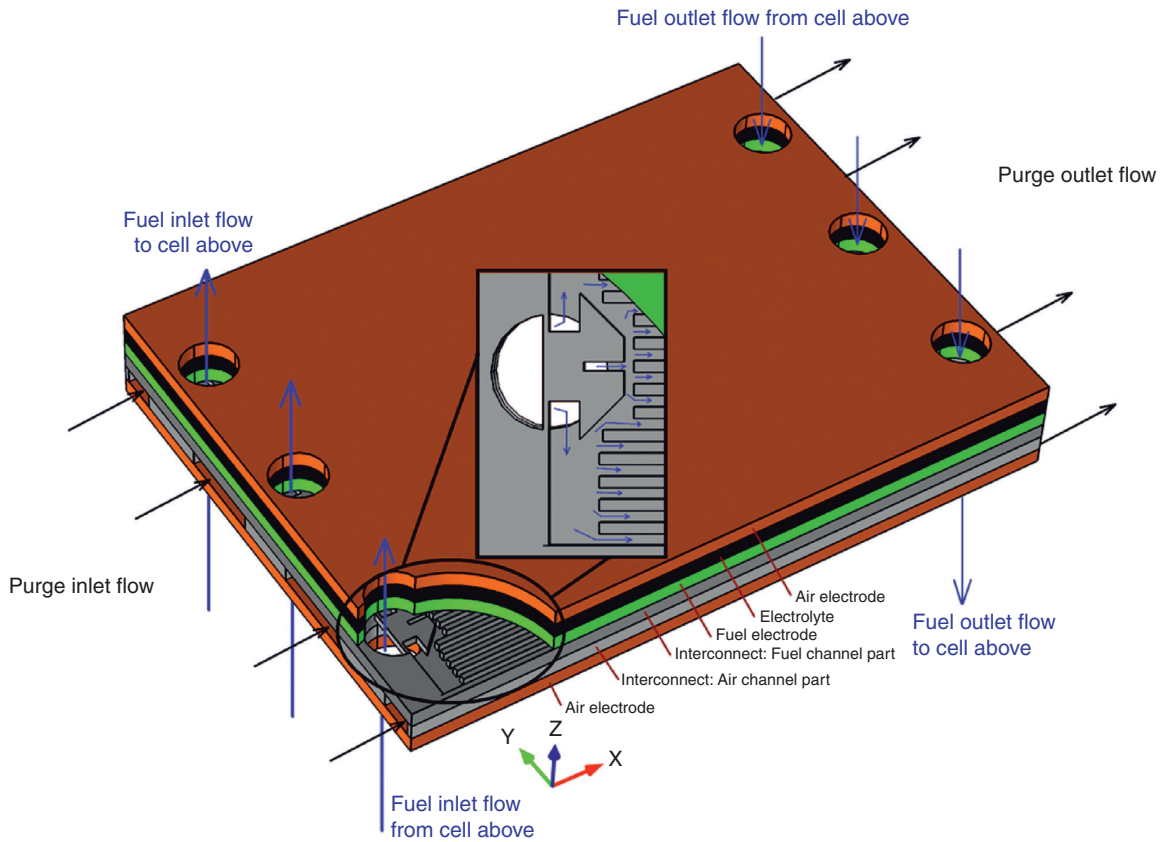

Fig. 14 Sketch of an SRU. The insert shows the gas distributor and the parallel channels. After [34] with permission from Elsevier.

A very important point is, however, that the chemical stability of 3YSZ is very poor in moist atmosphere and spontaneous phase transformation may occur within a few hours in the temperature interval of 100–200°C, with disintegration of the zirconia phase as a result [39]. This means that, during thermal cycling of 3YSZ, it must be protected by a dry atmosphere. Also, the high-temperature stability of the material was found to be limited.

Therefore, new material compositions for cell support were studied using CeO_2 as a co-dopant to Y_2O_3 in zirconia [40]. Various material compositions were analysed and optimized with respect to the structural stability for different sintering temperatures and new phase-stability diagrams developed. A new composition (NiO–1.5CeO_2:4.5$YO_{1.5}$-SZ) was found to be a superior composition, providing 30% higher strength than NiO–3YSZ at room temperature and 10% higher strength at 800°C. The main gain is a better chemical stability against degradation by moisture using a CeO_2-doped compound, although it is still susceptible to degradation in moist conditions at 100–200°C [40].

Water is also influencing the long-term stability of the zirconia through so-called slow (subcritical) crack growth, where water can act as a corroding agent at the crack tip, breaking chemical bonds (also referred to as stress corrosion). The phenomenon basically provokes crack growth below the critical (very fast) crack growth measured in most fracture-toughness measurements. This phenomenon has gained more attention over the years [42, 43] and recent works have characterized this phenomenon in greater detail [40, 44]. The stress-intensity factor to provoke a slow-growing crack can thus be as much as 30–40% lower than the fracture toughness [40], and this must be carefully considered as a design criterion.

Another recent important finding is that the main structural component of the fuel-electrode-supported cells, Ni(O)–YSZ, becomes considerably softer during the reduction period, allowing very fast creep in the structural parts of the composite [45]. The creep rate during reduction was measured to be between 7000 and 10 000 times faster than the creep rate during normal operation. This certainly is important for the stack assembly and reduction procedures, but it is also important for understanding the stress configuration inside the SOC stacks after reduction because the very fast creep is expected to reduce all residual stresses from TEC mismatches in the cell to zero at the point of reduction. Thus, to protect the electrolyte from compressive residual stresses, a reduction temperature above the operation temperature is preferred [45].

2.4 Cell degradation

The cell-degradation rate depends for a given cell and gas reactant mainly on the cell voltage/current density. Often, literature reports describe the degradation as being dependent mainly on current density, probably because most reported cell tests have been carried out in galvanostatic mode. Also, electrode overpotential is mentioned as important. Some inherent effects of current density and overpotential cannot totally be ruled out, but it seems that these claims are due to the fact that overpotential and current density are directly related to the electrode potential versus a reference electrode for each of the two electrodes. The electrode potential versus a well-defined reference is the main parameter that describes the thermodynamic state of a given electrode under given conditions. The Pt/O_2 (1 bar O_2, temperature) electrode is recommended as the common reference electrode for SOC electrodes, even though these electrode potentials are usually not directly available, but have to be calculated from electrochemical characterization of a cell (see e.g [46] for a procedure). Recent tests have proven that the outcome of durability results is dependent on the test mode (galvanostatic or potentiostatic) [31]. This is a consequence of the importance of the electrode potential, as explained below. Furthermore, alternating the reversal of the current, i.e. changing the test mode from electrolysis to fuel cells forth and back, may almost stop the cell degradation (see below).

Figs 15 and 16 illustrate the most common electrical-potential-driven degradation mechanisms of the common SOC electrodes and electrolytes. In the case of the Ni–SZ (stabilized zirconia) cermet (Fig. 15), a very negative electrode potential reduces the zirconia into Zr metal, which dissolves in the Ni, and the tendency is that this will end up causing zirconia nanoparticles, which will block the Ni–SZ contact and thus the reduction of H_2O and CO_2, but, if the reduction of the cermet can be done gently enough, then the nanoparticles may for a while improve the electrode performance.

The nanoparticles are formed at relatively positive electrode potentials (up to approximately –1.4 V versus 1 bar O_2, 800°C) compared to the thermodynamically calculated potentials mentioned above. This will be discussed further below.

At very positive potential, the Ni is oxidized to NiO, which initially is formed as nanoparticles. In a kind of analogy to the SZ-reduction case above, a slow, short oxidation of Ni may temporarily activate the electrode. If the oxidation of Ni is continued, this will damage the electrode irreversibly, especially if the reduction–oxidation of Ni happens many times (redoxing); the cermet will be mechanically destroyed because of the large volume difference between Ni and NiO. After the re-reduction of NiO to Ni, the fast self-diffusion of Ni causes the Ni particles to coarsen. Some of the Ni particles will grow until their growths are stopped by the SZ. Then, during the next oxidation of Ni to NiO, further volume expansion takes place and so on.

A strong reduction will decompose perovskite and other possible oxide electrodes (Fig. 16). The initial stage of this breakdown is a formation of nanoparticles, which will reform the electrode-material composition, but keep the nanoparticle form for a while. Again, such nanoparticles

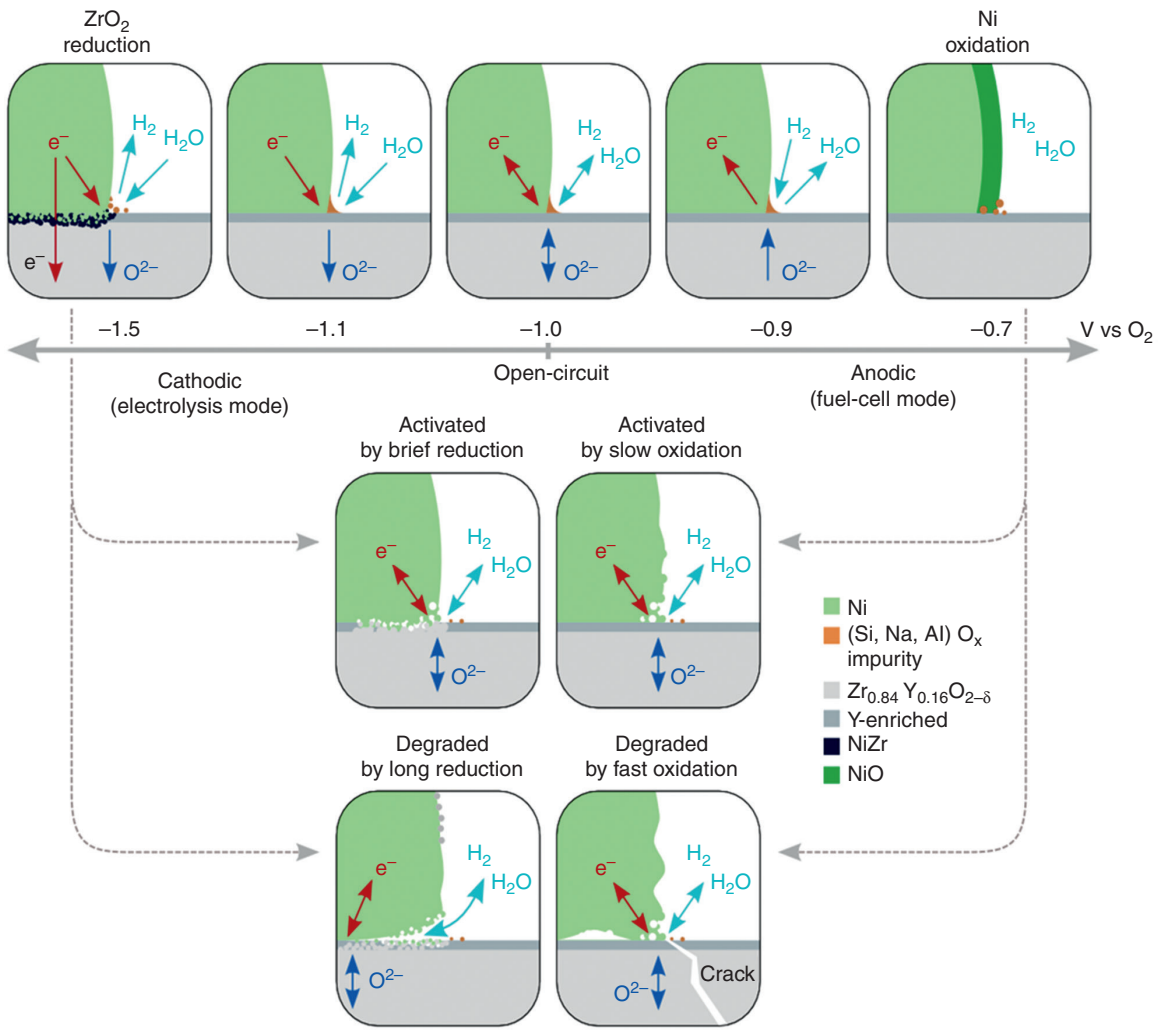

Fig. 15 Commonly seen Ni–YSZ fuel-electrode-potential-driven activation and degradation phenomena that affect the Ni/YSZ/H_2,H_2O or CO/CO_2 three-phase-boundary (3PB). From ([47]) with permission from Springer.

will increase the electrode performance. At high positive potential, O_2 bubble formation in grain boundaries with weakening of YSZ near LSM at 'high' oxygen-electrode overpotential occurs [48]. Here, 'high' anodic overvoltage may actually start at ~60 mV at 850°C (Ebbesen, **unpublished** work [49]).

2.4.1 *Degradation of Ni–YSZ electrodes with high cathodic overpotential*

In this section, the various kinds of degradation of the Ni–YSZ cermet electrode are summarized.

2.4.2 *Electrode-potential-driven loss of contact*

This kind of degradation is typically taking place within the first 1000 h of test at current densities above around 1 A cm^{-2} in good cells, i.e. Ni–YSZ electrodes at a potential in the range of approximately –1.2 to –1 V versus Pt/O_2 (1 bar, 800°C). The phenomenon is summarized below. It is described in more detail in [50, 51]. However, the possible threshold value, above which this occurs, is not well determined and more work on this is definitely needed.

Fig. 17 shows the appearance in SEM pictures of the Ni–YSZ electrode part next to the electrolyte. It displays the structure of a non-tested electrode, of an electrode at gas inlet and outlet after tests during 678 h, and of one at inlet and outlet after 138 h at –2.0 A cm^{-2} in co-electrolysis mode. Our hypothesis—illustrated in Fig. 18—is that the Ni migration starts due to loss of contact between Ni and YSZ particles.

The loss of contact was in a previous hypothesis assumed by some of the present authors to be caused by the positive free energy of the formation of Ni–YSZ interfaces in the strongest polarized part of the Ni–YSZ electrode [50], but this may not be the main reason. Furthermore, the previous hypothesis predicted only Ni migration in the case of steam electrolysis, but now similar Ni migration has been observed to occur also in steam-free CO_2 electrolysis [52]. YSZ nanoparticle formation is proposed in our modified hypothesis to be due to thermomechanical breakdown of YSZ into nanoparticles at the Ni–YSZ 3PB [53], but, before describing this in slightly more detail, the observations of YSZ nanoparticles are presented.

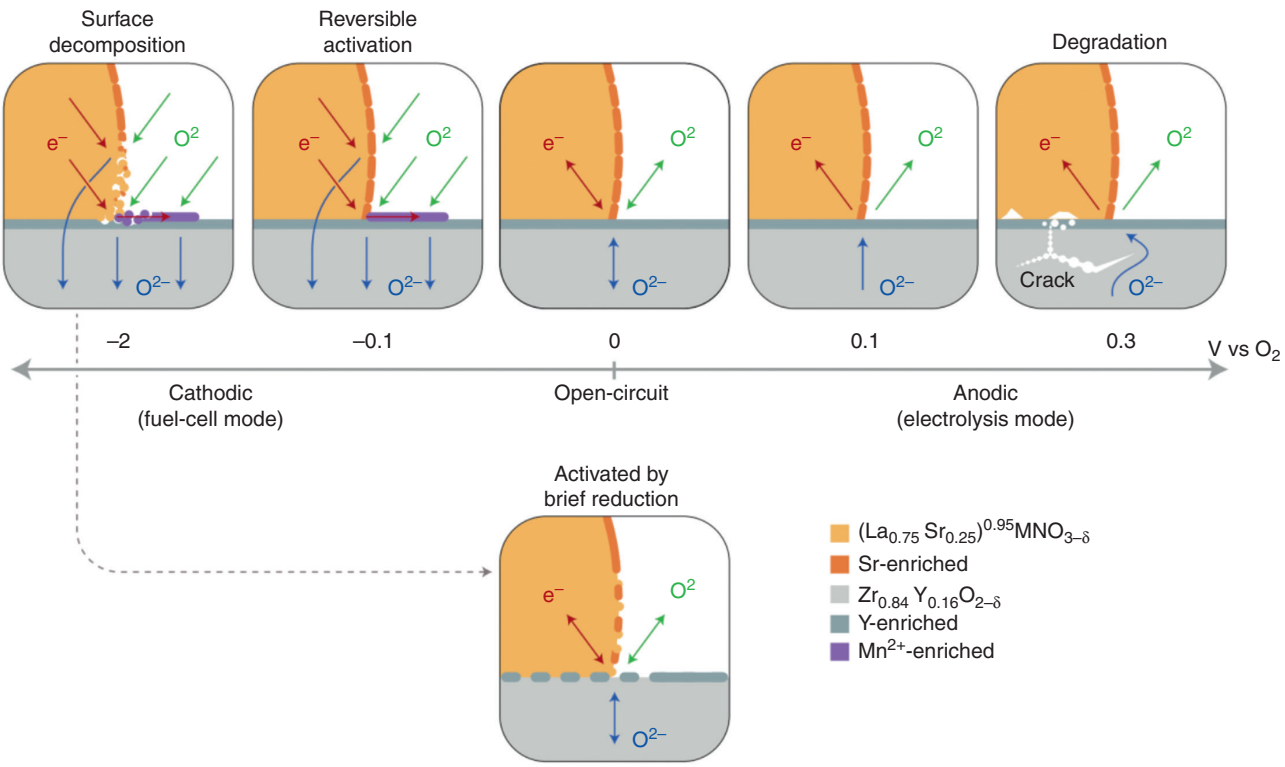

Fig. 16 Commonly seen perovskite oxygen-electrode-potential-driven activation and degradation phenomena of the LSM/YSZ/O_2 3PB. Other perovskite oxygen electrodes exhibit the same activation and degradation mechanisms as LSM at high negative and at high positive potentials but then naturally without Mn^{2+} spreading. Mixed ionic-electronic-conductor (MIEC) fuel electrodes generally show considerable activation under moderate cathodic polarization. From [47] with permission from Springer.

2.4.3 *Formation of zirconia nanoparticles around the Ni particles during SOEC operation*

As indicated in Fig. 15, the Ni–YSZ electrode may be destroyed at highly negative Ni-electrode potentials. It was hypothesized that electrochemical reduction of ZrO_2 (from YSZ) occurred and was dissolved into a dilute (1 p.p.m.) Zr solid solution in Ni and formed Ni–Zr compounds at more negative potential. It was further hypothesized that, during a following re-oxidation of Zr to ZrO_2, when the contact between Ni and YSZ is lost, nanoparticles are precipitated around the Ni particles [35].

Fig. 19 gives the test history of the worst case observed at DTU and Fig. 20 shows SEM micrographs of the tested electrode.

A mechanism of this process is described in detail [35]. From thermodynamics of pure bulk materials, a potential of 1.52 ± 0.16 V versus O_2 (1 bar, 850°C) was calculated in order to dissolve 1 p.p.m. Zr in Ni [54]. In the case of Fig. 19, the onset of degradation starts at a cell voltage of 1.13 V, which means a Ni potential of about –1.05 V, as the voltage drop at the O_2 electrode plus the loss through the electrolyte is about 0.1 V. Thus, this is in the lower end of the simulated range. Experiments with a Ni wire in contact with YSZ at 900°C revealed that no observable reduction of Zr into Ni takes place before the Ni-electrode potential is more negative than apporximately –2 V versus O_2/Pt (1 bar, 900°C) and, even at such negative potentials, no substantial amounts of YSZ nanoparticles were observed [36]. Thus, it seems that another hypothesis for the formation of YSZ nanoparticles is needed.

The above hypotheses are valid for H_2O-containing atmosphere. However, a similar phenomenon has recently also been observed in dry CO_2/CO atmosphere during CO_2 electrolysis. This and the formation of zirconia nanoparticles far inside the stability range of YSZ require a different hypothesis.

2.4.4 *New hypothesis for Ni–YSZ loss of contact and Ni migration*

It appears that the loss of contact between Ni and YSZ is a prerequisite for Ni migration in Ni–YSZ composite electrodes and, when the Ni–YSZ contact is lost, then the Ni will start migrating, which will cause a loss of contact between Ni particles [50].

YSZ nanoparticles have been observed at the interface between Ni and YSZ particles and on the surface of Ni particles in Ni–YSZ electrodes tested with cell voltages below 1300 mV for more than 1000 h [35]. As mentioned, the formation of the nanoparticles occurs at an electrode potential well within the chemical-stability window and they occur primarily near the electrolyte|electrode interface [35]. For composite electrodes, a cathodic polarization of 160–300 mV is required to initiate the loss of Ni–YSZ interfacial contact at the 3PBs at 800°C and 90% steam as inlet

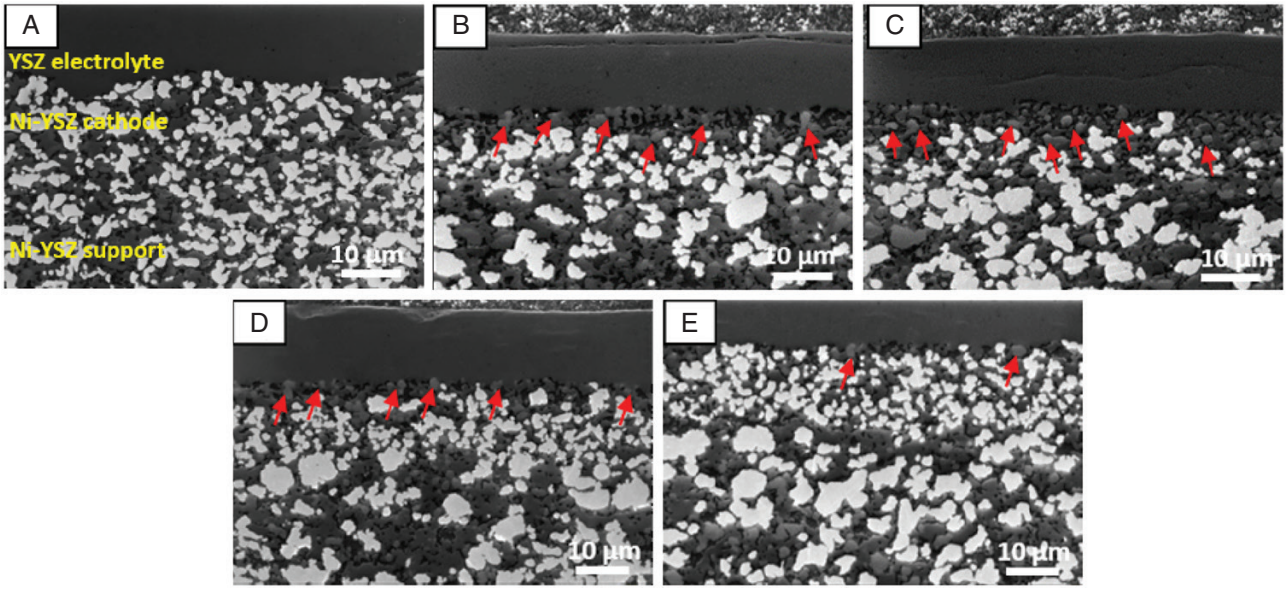

Fig. 17 Low-voltage SEM micrographs of a fine-structured Ni–8YSZ active electrode between the coarse 3YSZ support and the 8YSZ electrolyte. (a) not tested, (b) H_2O–H_2 inlet and (c) outlet tested for 678 h, (d) inlet and (e) outlet tested for 138 h. Bright: interconnected Ni; light grey: non-connecting Ni; dark grey: YSZ; black: pores. Red arrows point to uncontacted Ni. 865°C increasing to 875°C. Inlet gas: 45% H_2O + 45% CO_2 +10% H_2, –2.0 A cm^{-2}, 60% (steam + CO_2) conversion. From [51]. Permission from Elsevier.

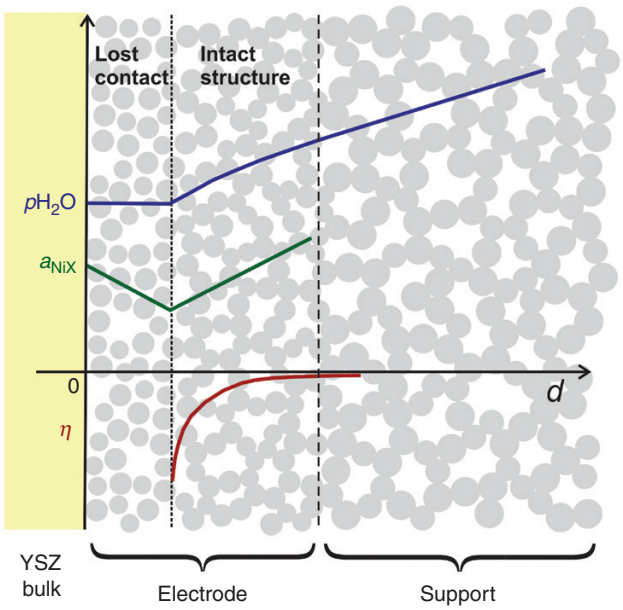

Fig. 18 A sketch of the qualitative variation of the three important parameters from the surface of the bulk electrolyte (d = 0) through the two zones of the as-fabricated SOEC active cathode (Electrode), which has been separated into a zone with partially lost contact between Ni and YSZ particles and a zone with intact structure. d is the distance from the bulk YSZ electrolyte, η is the local overvoltage of Ni particles, a_{NiX} is the activity of NiX species and pH_2O is steam partial pressure, which is indicative of the redox potential. Modified after [50] with permission from Wiley.

gas [11, 55]. CGO infiltration in Ni–YSZ composite electrodes is observed to impede the Ni migration [56].

A hypothesis explaining these observations is provided below.

During the electrolysis of steam in a Ni–YSZ electrode, two types of heat are generated. One is Peltier heat ($-T\Delta S$) and the other is Joule heat. In a mixture of 98% H_2 and 2% H_2O, at 1000°C, the Peltier heat produced is 41 kJ/mol e^- [57]. This corresponds to a cathodic polarization of 425 mV. The Peltier heat increases with decreasing H_2O concentration and, combined with the Joule heat, the heat evolution during electrolysis causes steep thermal gradients at the 3PB. The width of the 3PB is only a few nm and preliminary calculations indicate that temperature gradients of more than 10^{4}°C cm^{-1} are present at the gas|Ni|SZ 3PB. Similarly to any other ceramic material, YSZ expands with increasing temperature and, due to brittleness, it cracks once the thermomechanical stress caused by the steep thermal gradients exceed the differential fracture energy. This may explain why a certain cathodic polarization is required for the loss of Ni–YSZ contact at the 3PBs with the following initiation of Ni migration.

Due to the gradient in the Galvani potential (also called electrostatic potential), which is a consequence of the relatively low O^{2-} conductivity compared to the high conductivity of Ni, the current density is largest near the electrode|electrolyte interface. Gas-diffusion limitations make the H_2O and CO_2 concentrations lowest near this interface, which means that the Peltier heat production is highest near the interface. This is hypothesized to cause YSZ fracturing and the formation of nanoparticles near the electrode|electrolyte interface is in agreement with the experimental findings [35]. If the current is reversed, then the Peltier heat decreases due to increasing H_2O concentration at the 3PB, and further the Peltier heat is negative and counterbalances the Joule heat. Therefore, nanoparticle formation is only observed in electrolysis mode.

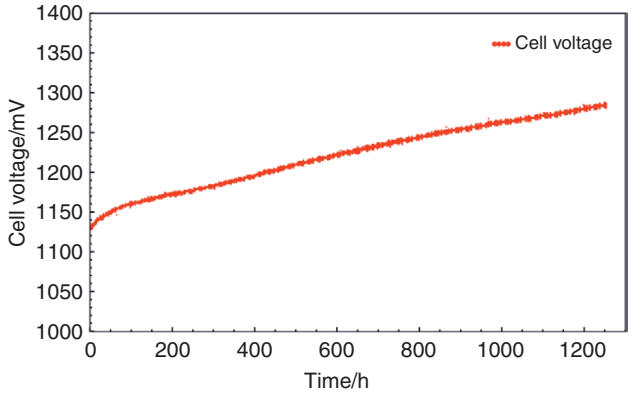

Fig. 19 Cell voltage as a function of time for a less durable SOEC. 850°C, 10% H_2 + 45% H_2O + 45% CO_2 to Ni–YSZ electrode; current density –1 A cm^{-2}; reactant conversion degree 62%. Modified from [35] with permission from Electrochemical Society.

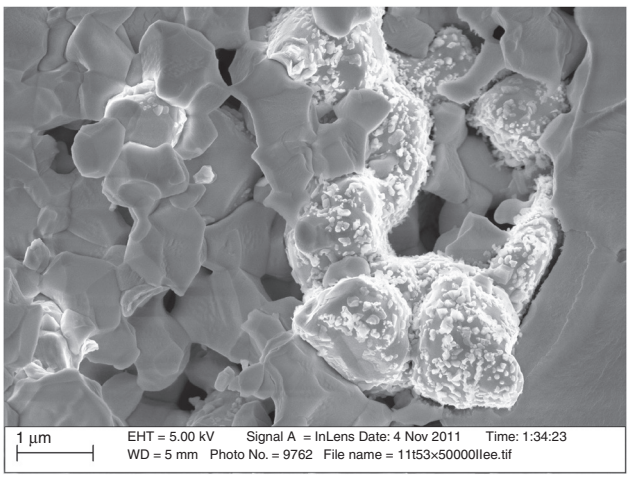

Fig. 20 SEM of Ni–YSZ cermet after the test in Fig. 19. Detrimental nanoparticles of ZrO_2 formed on Ni particle surfaces are breaking electrical contact with YSZ [35]. With permission from Electrochemical Society.

Ni migration is reported to be of similar magnitude in H_2O/H_2 and CO_2/CO gases [52, 58, 59]. The concentrations of Ni-containing species in the Ni–O–H gas-phase system seem low if such species should explain the observed Ni-migration rate [60]. Further substantial differences in the activity of Ni-containing species in the Ni–O–H and Ni–O–C gas-phase systems and the chemical activity of these are all very low. All in all, this suggests that NiX compounds with activities above 10^{-7}, X being impurities like P and As in sub-p.p.m. concentrations [61], may be involved in the Ni migration.

Once the Ni and YSZ contact has been broken, the electrochemical conversion of H_2O and/or CO_2 stops. Due to limited surface and gas diffusion, the partial pressure of H_2O and/or CO_2 in the gas phase increases near the broken 3PBs and the concentration of mobile (adsorbed and volatile) Ni (impurity) species increases. The concentration gradient of mobile Ni (impurity) species causes Ni to migrate towards the still active 3PBs, i.e. to migrate *away* from the electrolyte|electrode interface.

2.5 Prevention of cell degradation

A good point is that, in energy applications, it is in principle possible to counteract the cell degradation by alternating operation in SOECs and SOFCs, as the cells are reversible, and so are the initial stages of several of the degradation mechanisms as revealed in Fig. 21. This may soon become very important for the commercialization of SOCs.

2.6 Electrode poisoning

RSOCs are sensitive to a number of poisons like other electrolysis and fuel cells. Differently from the low-temperature fuel cells, RSOCs are sensitive to the poisoning effect of some trace impurities in the raw materials of the cell components, but also RSOCs in both modes are sensitive to a number of gaseous impurities such as compounds of B, S, P, As, Cl and Cr [14, 29, 63]. Some methods of mitigating the poisoning problems have been found (see e.g. [64]), but it is still an issue with respect to the extra cost of SOFC technology.

2.6.1 *Fuel electrodes*

In particular, the 3PB in the Ni–YSZ electrode is sensitive to becoming blocked by the segregation of glassy SiO_2 together with Na_2O and many other trace (a few p.p.m. level) impurities in YSZ and Ni [65]. Here, it plays a role that the slightly volatile $Si(OH)_4$ forms even at high temperature and may migrate downhill on pH_2O gradients in the steam-containing gas phase. Thus, RSOCs are much more sensitive to this in SOEC mode than in SOFC mode, even though glassy silica certainly may block 3PBs in SOFC modes also [66–68].

No general measure against this has been demonstrated clearly apart from keeping the raw materials very clean. However, this may be very expensive. It seems that it is better to figure out how to handle the poisoning trace impurities rather than carry out ultra-cleaning of raw materials and processing, e.g. by using 'scavengers'. In the case of silica, additives of temperature-stable alkaline oxides such as SrO, La_2O_3 and partially reduced CeO_2 (or $Ce(IV)_{1-x}Ce(III)_xO_{2-px/2}$) may be good scavengers of the acidic SiO_2. The positive effect of infiltration with ceria into the Ni–YSZ electrode may at least partly be due to a scavenging effect of Ce^{3+} by reacting with the glassy silica and forming crystalline $Ce_2Si_2O_7$. The glassy stuff seems to be smeared out around the 3PB, while separate particles of crystalline material are not expected to block gas access to 3PB to any large extent.

The Ni–YSZ electrode is also sensitive to a number of gaseous compounds. Sulphur seems to be a very abundant impurity, as most H_2 today is derived from fossil fuels, and therefore the effect of S-compounds has been widely investigated.

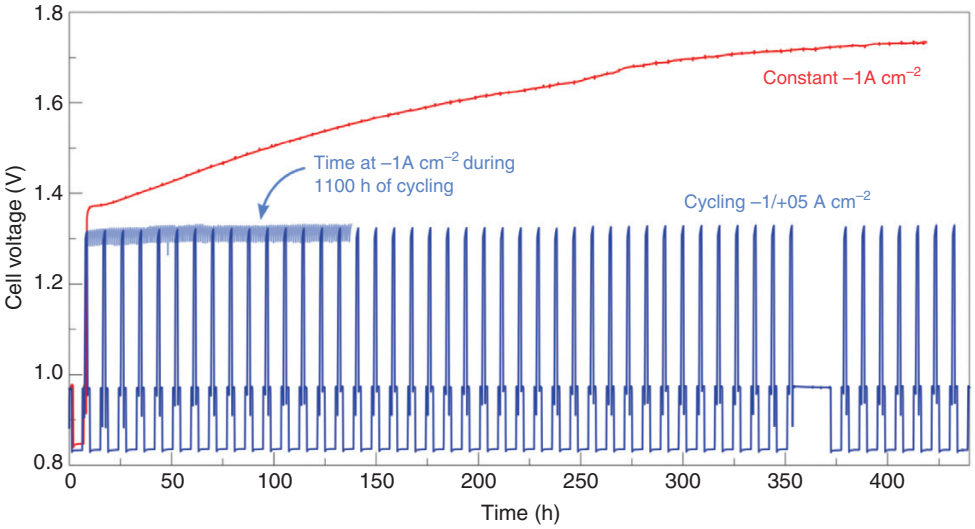

Fig. 21 Reversible operation. SOC stability during constant current-density (–1 A cm^{-2}) electrolysis test compared to reversible-cycling test of 1 h electron conductor (EC) (–1 A cm^{-2}) + 5 h fuel cell (FC) (+0.5 A cm^{-2}). During open-circuit and FC mode, ~25 L h^{-1} of $pH_2/pH_2O \approx 50/50$ and EC mode ~13 L/h of $pH_2/pH_2O \approx 10/90$ gas was supplied. Pure O_2 at the O_2 electrode [62]. With permission from Springer.

According to Hansen and Rostrup-Nielsen [69, 70], S-containing impurities will usually dissociate at RSOC operation temperatures (>700°C) and atomic S will adsorb on active sites on the Ni surface, and thereby block the electrochemistry. The S adsorption on Ni has been found to follow a Temkin isotherm in H_2-containing gas, i.e. the enthalpy of the adsorption of sulphur varies linearly with coverage, and the performance degradation is proportional to the sulphur coverage. Further, they report that, in SOFC mode with a cell voltage of 0.7 V in the temperature range of 700–900°C, a coverage threshold of ~0.6, below which there is no effect on H_2 oxidation, is found. Based on the formula given in [69]:

$$\theta_S = 1.45 - 9.53 * 10^{-5}T + 4.17 * 10^{-5}T * \ln\left(\frac{p(H_2S)}{p(H_2)}\right) \quad (8)$$

Plus, assuming $pH_2 = 0.5$ bar and 800°C, we find that this threshold in S coverage is equivalent to $pH_2S = 3{\cdot}10^{-8}$ bar or 0.03 p.p.m. Even though this is a very low, it also means that it is possible to clean a gas sufficiently by passing it over a Ni-containing filter like powdered Ni–YSZ cermet or a pre-reformer catalyst at 500°C or just slightly lower than the RSOC operation temperature. Also, in the case of the electrolysis of dry CO_2 without any H_2, a Ni–YSZ electrode will become poisoned by any S level if exposed for a long enough time. It was observed experimentally that CO_2/CO gas with S trace levels as low as ~1 p.p.b. ($pH_2 = 10^{-9}$ bar) gradually poisoned the Ni–YSZ electrode over 500 h but, when the gas was cleaned through a filter of Ni–YSZ cell support material, no measurable degradation was observed over 500 h [71].

An interesting observation regarding the effect of exchanging YSZ with ScYSC in the Ni-cermet electrode is that apparent differences in S-poisoning resistance between cell types have shown up to be caused by differences in cell performance. Cells with Ni–YSZ electrodes were optimized by the improvement of the structure to the same electrochemical performance level as the Ni–ScYSZ electrodes, which had superior resistance to S poisoning apart from their better electrochemical performance. Then there was no measurable difference between the two cell types [72]. This indicates that RSOCs with good initial electrochemical performance degrade less than cells with bad initial performance at a given current density. This has probably to do with the overvoltage difference between good and bad electrode structures in galvanostatic testing.

Another way to avoid the S poisoning of Ni is naturally to use other materials than Ni and YSZ, or adding additives. Examples are to change to Ni–CGO or to add nanoceria to Ni–YSZ, or to change both Ni and YSZ to e.g. doped strontium titanates or $La_{1-x}Sr_xMn_{1-y}Cr_yO_3$ (LSCM). Not surprisingly, all other materials have their pros and cons and much more about this can be found in other reviews and textbooks [7, 10, 29, 63, 64].

2.6.2 *Oxygen electrodes*

Poisoning of the RSOC oxygen electrodes has been studied much less than the fuel-electrode poisoning, probably because oxygen-electrode poisoning has not been a big problem in laboratory tests. The poisoning by Cr(VI) oxides and oxyhydroxides is the most studied [14, 63, 73–75] because this problem appeared when stack building with interconnects of ferritic stainless steel such as Crofer became popular. Step one of the reaction that takes place on the top of the Cr_2O_3 passivating layer is an oxidation of the Cr(III) in the top of the solid Cr_2O_3 to Cr(VI) compounds in the gas phase. In dry air, CrO_3 is formed and, in moist air, a mixture of CrO_3 and $CrO_2(OH)_2$. Over a cathodically polarized O_2 electrode, the Cr(VI) compounds will be reduced to solid Cr(III) compounds on the active sites at the 3PBs,

which get blocked, and the electrode performance will decrease quickly with increasing current density. However, chromium poisoning may also take place at OCV and under anodic polarization in SOEC mode, but at a significantly lower rate. The reason is that the acidic Cr(VI) compounds will react with the SrO content of the perovskite electrode materials, forming chromates by reactions such as

$$SrO\,(solid) + CrO_3\,(gas) \rightleftharpoons SrCrO_4\,(solid) \quad (9)$$

As this reaction is a purely chemical reaction, it is not directly affected by the electrode potential and it will not preferentially block the 3PBs at OCV and anodic polarization. Under these conditions, all of the surface of the Sr-containing perovskite will be attacked.

The main measure against chromium poisoning is to cover the surface of the chromium-containing steel with a suitable metal oxide. The spinel-structured $Mn_{1.5}Co_{1.5}O_4$ seems to make a coating that is effective in preventing chromium evaporation from the steel surface [76] and has become a popular coating.

Other compounds that may affect perovskite-type oxygen electrodes negatively are SO_2, H_2O and CO_2. According to a review by Jiang [14], SO_2 also reacts with the SrO content of LSCF electrodes, resulting mainly in $SrSO_4$ above and SrS below ~700°C, and LSCF electrodes are most susceptible at about 700°C. The oxygen surface exchange rate is reported to decrease by two orders of magnitude after exposure to 20 p.p.m. SO_2 at 700–900°C for 2 days. As SO_2 is a common pollutant in air (around 20 p.p.b. in cities), it may be necessary to clean the air feed to the O_2 electrode in an SOFC.

The review by Jiang also deals with the effects of CO_2 and H_2O and reports that, while an LSCF electrode seems resistant to CO_2 and H_2O above 750°C, it showed severe degradation at 600°C in an atmosphere of 2.8% CO_2 plus 2.6%H_2O in O_2 with indications of formation of $SrCO_3$.

2.7 Carbon deposition in Ni–YSZ SOC electrodes

Ni is an excellent catalyst for carbon formation [77]. The deposition of carbon in the form of carbon nanotubes [78–81] (CNTs) (see Fig. 22) in the porous structure can fracture the electrode (see Fig. 23) leading to rapid failure of the device [82, 83]. To avoid this, it is highly important to understand when and how the electrode is at risk of carbon deposition.

One must distinguish between the operation with the two relevant carbonaceous gases, i.e. methane (CH_4) and carbon monoxide (CO), as well as for the two different operating modes, i.e. in fuel-cell mode as an SOFC and in electrolysis mode as an SOEC. Deposition of carbon can primarily occur by two different reactions:

$$2\,CO\,(g) \rightarrow C\,(s) + CO_2\,(g) \quad (10)$$

$$CO\,(g) + H_2\,(g) \rightarrow C\,(s) + H_2O\,(g) \quad (11)$$

These are known as the Boudouard reaction and the reverse coal-gas reaction, respectively, both of which become favourable at lower temperatures. In addition to these reactions comes the decomposition of hydrocarbons, which, however, is less relevant for SOCs, since the hydrocarbons are typically reformed prior to carbon deposition taking place. Furthermore, there have been speculations that the electrochemical reduction of CO(g) and CO_2(g) directly to C(s) is possible [84].

Electrolysis of CO_2 into CO or of H_2O/CO_2 into H_2/CO (syngas) can result in carbon deposition at the interface between the electrode and the electrolyte [82–84]. Thermodynamics dictates the onset, as shown in the C–H–O ternary diagram in Fig. 24. Alternatively, one can also consider the voltage of the cell, as shown in Fig. 25, where it becomes apparent that carbon deposition can occur at a sufficiently high overpotential. Degradation

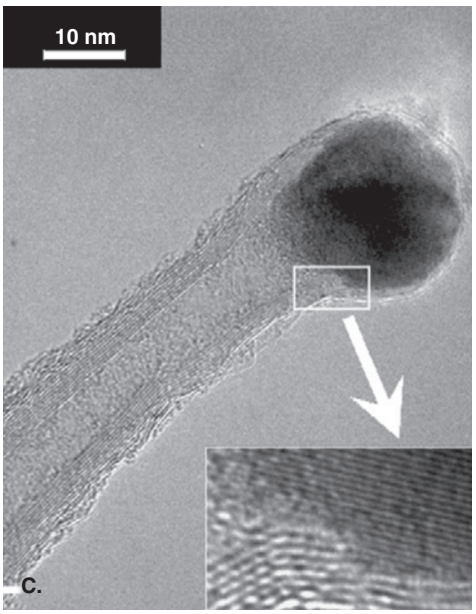

Fig. 22 Carbon nanotube initiated by a nickel particle being lifted out of position (tip-growth). Image is reproduced with permission from Elsevier [79].

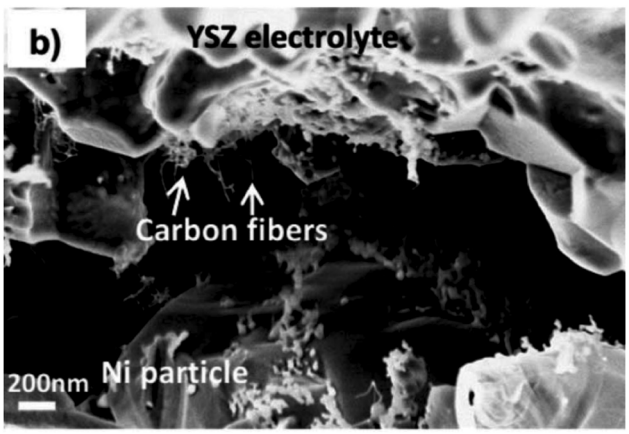

Fig. 23 Carbon fibres fracturing the porous electrode during co-electrolysis. Image is reproduced with permission from Electrochemical Society [82].

of the electrolysis cell by other means, e.g. impurity poisoning, may then eventually lead to carbon formation [85], which will cause a sudden failure. Furthermore, gradients of temperature, gas composition and the overpotential must be taken into account, since the local conditions at the reaction site govern whether carbon deposition will initiate [83, 86, 87].

Contrarily, operation in fuel-cell mode with CH_4 can result in carbon deposition at the electrode surface. This is typically less destructive, since carbon can grow into the gas channels, and since the nature of the operating mode is to oxidize the gas atmosphere. Operating just beyond the onset, carbon will deposit at OCV but, when drawing a current, the carbon is oxidized and steady operation can be expected [89]. This is, of course, a risky strategy, as, in the event of a power failure, carbon deposition at OCV may destroy the cell. CH_4 is typically reformed either externally or internally directly in the electrode via the reverse-methanation reaction:

$$CH_4 + H_2O \leftrightarrow CO + 3H_2 \quad (12)$$

The product can then yield carbon deposition on account of either Equation (10) or Equation (11). Reports in the literature of carbon deposition during fuel-cell mode are plentiful and a complete review is beyond the scope of this paper, so the reader is referred to the review by Boldrin et al. [64].

The most popular pathway for mitigating the issue is substituting Ni (or doping the electrode) with ceria [84, 90–94]. The mechanism for the increased tolerance is linked to the presence of oxidized carbon intermediates, which energetically trap the carbon before forming destructive CNTs. It has been suggested that this enables a reversal of Equation (10) on the ceria surface [94]. Other

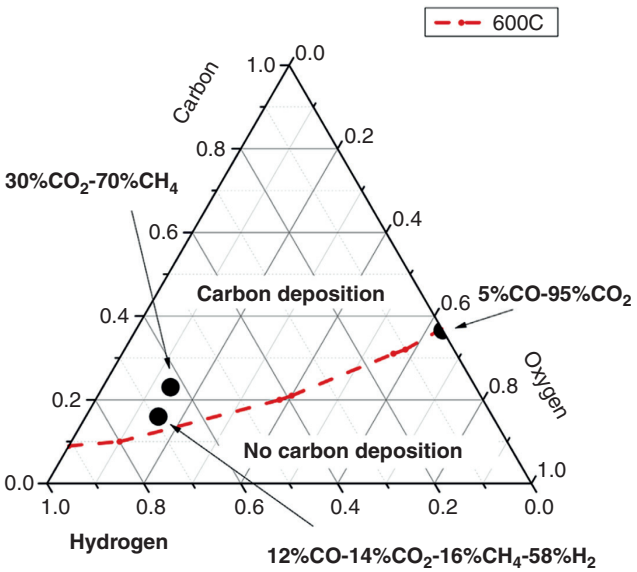

Fig. 24 C–H–O ternary diagram with operation at 600°C indicated by the red, dashed line. A few specific gas compositions are indicated. Reproduced with permission from Elsevier [88].

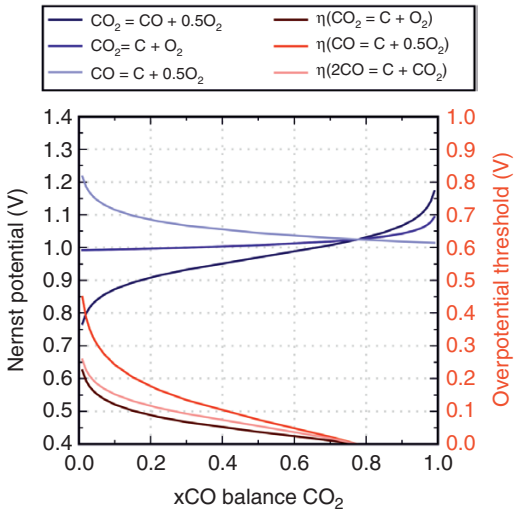

Fig. 25 Nernst potential at 750°C for Equation (7) and the reactions of direct electrochemical reduction of CO and CO_2 to carbon, against the gas composition during CO_2 electrolysis. The second y-axis indicates the overpotential that will initiate carbon deposition. Reproduced with permission from Elsevier [83].

interesting mitigation strategies are doping with more carbon-tolerant metals [88, 91, 95, 96], passivation with sulphur [83, 97], exsolution of the Ni particles [98], flowing excess oxidizing gas [99] or applying a positive bias [99], as mentioned earlier.

2.8 SOEC-operation strategies

2.8.1 *Stack performance and durability criteria*

RSOC stack and system manufacturers must have criteria for an SOC stack that can pass the criterion of acceptable operation. One is that the performance must be constant, i.e. a specified power (a given number of watts) put into the SOEC stack must give at least the production rate of CO and/or H_2 that was promised, and a given fuel input into an SOFC must give a minimum of the promised watts. This may in practice be done by starting the stack life at 700°C and then use increasing temperature to compensate for the degradation. The end-of-life criterion may then be set as reaching 825°C because, above this temperature, the commonly used interconnector plates of ferritic stainless steel will oxidize very quickly, and full oxidation of the interconnector plates means that the stack will be destroyed. Both the start and the end temperature may naturally be changed by the development of better cells and stacks.

2.8.2 *Gas-product quality*

Another criterion is the quality of the H_2 and/or the CO, which is paramount in chemical-industry application with on-site production of CO. This means that mechanical integrity is most important, i.e. almost no cracks or holes in the electrolyte, the interconnector plates or the seals can be allowed.

As air or N_2 may be used as a sweep gas on the oxygen side, it is possible to calculate the allowed leak rate of air and/or N_2 though the electrolyte, the interconnect and the seals, when the maximum accepted level of N_2 in the CO product gas has been decided.

3 New types of RSOCs

The conventional Ni–YSZ composite electrode (Fig. 26a) has been microstructurally optimized over many years to provide high reaction rates. However, it is also one of the most common sites of performance degradation, resulting from the high mobility of Ni, the susceptibility of Ni/YSZ/gas 3PBs to poisoning by impurities from the gas supply or from the cell raw materials, carbon deposition on Ni and other degradation mechanisms. Furthermore, state-of-the-art oxygen electrodes have electrode polarization resistance (RP) values of less than half the ~0.1 Ω cm^2 achieved with state-of-the-art Ni–YSZ at 700°C in H_2/H_2O [100–102].

For more than 25 years, research has sought to replace Ni–YSZ with alternative materials that avoid these degradation issues while providing similarly low RP. Most efforts have focused on discovering single-phase mixed ionic-electronic conductor (MIEC) oxide materials, which provide electrochemical reaction sites on the entire surface/gas two-phase boundary (2PB), making them less susceptible to blockage by impurities than 3PB-based electrodes (Fig. 26b). One of the earliest MIEC electrode materials is CeO_2 doped with Gd, Ca or Nb, first investigated in the early 1990s [104, 105] and still under development today [103]. Doped ceria has long been considered as an electrolyte material, where its substantial electronic conductivity is a problem and causes loss of cell-energy efficiency. However, its electronic conductivity is too low for a single-phase electrode. Nevertheless, this fluorite structured MIEC appears very promising as an electrocatalytic component of a composite electrode where another material provides sufficient electronic conductivity, as discussed further below. Most investigated single-phase MIEC electrodes are perovskites or double-perovskites with much higher electronic conductivity, such as $La_{0.75}Sr_{0.25}Cr_{0.5}Mn_{0.5}O_{3-\delta}$ [106], $(La,Sr)(Cr,Fe)O_{3-\delta}$ [107–109], $Sr_{2X}MoO_{6-\delta}$ (where X = Mg, Mn, Ni, Fe, etc.) [110–112], $SrFe_{0.75}Mo_{0.25}O_{3-\delta}$ [113, 114] and $PrBaMn_2O_{5+\delta}$ [115, 116]. These materials show differing levels of compatibility with electrolyte materials like YSZ and varying performance, approaching that of Ni–YSZ, but still with RP >0.3 Ω cm^2 at 700°C in H_2/H_2O.

Unfortunately, although some of these oxides approach Ni–YSZ performance, all exhibit orders of magnitude lower electronic conductivity than Ni, often <10 S cm^{-1} for the bulk material and an order of magnitude lower for a porous electrode made of the material, which adds ohmic resistance and makes electronic current collection challenging. Additionally, MIECs often present mechanical weakness due to their thermal- and chemical-expansion behaviour. Therefore, a wide variety of composites have been investigated, with similar separation of functions as in Ni–YSZ, in which Ni provides electronic conductivity and catalytic activity and YSZ provides ionic conductivity. Electron conductor (EC) alternatives to Ni include other metals such as Cu and Ag, some of the perovskites mentioned above and other perovskites that are almost pure ECs, not MIECs, such as $SrTiO_3$ doped with La, Y or Nb. Cu and other low-cost metals show comparably high electronic conductivity to Ni, but they have lower melting points and are unfortunately even more mobile than Ni. Classical composite structures like doped $SrTiO_3$ with doped CeO_2 have been tested but lack electrocatalytic activity, at least in part because around half of the electrochemically active doped CeO_2 surface area has been replaced with relatively inactive doped $SrTiO_3$ surfaces (Fig. 26c) [117].

An alternative, promising composite electrode architecture is based on porous ion-conducting backbones or scaffolds such as YSZ or $La_{0.9}Sr_{0.1}Ga_{0.8}Mg_{0.2}O_{3-\delta}$ or MIEC backbones such as doped CeO_2. After the high-temperature sintering stage to produce these porous substrates, ECs and electrocatalysts are added by the infiltration of metal precursor salt solutions that produce metal or metal-oxide coatings upon heat treatment at a lower temperature than the initial sintering temperature (Fig. 26d) [118]. This allows the use of materials that would react or decompose at the higher sintering temperatures and the ability to retain nanoparticles during the lower-temperature heat

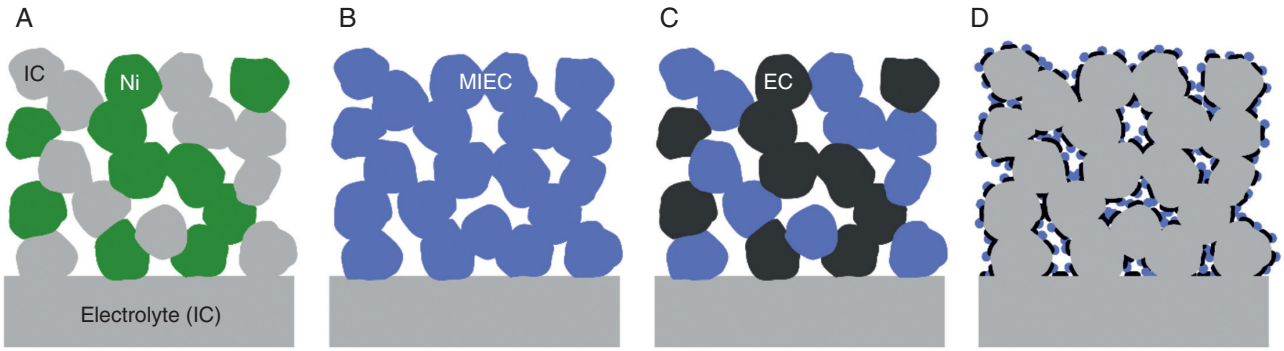

Fig. 26 Comparison of porous-fuel-electrode materials and structures, adapted from [103]. The component materials in each diagram (a)–(d) share the same colours. With permission from Electrochemical Society.

treatment. This backbone architecture is also a nearly optimal structure, as can be seen via porous electrode modelling, with the backbones providing large highways for ion transport, extending the reaction zone far from the electrolyte into the electrode thickness. Indeed, ion-conducting backbones coated with dispersed doped CeO_2 nanoparticles and/or Ni or other EC show performance that matches or exceeds Ni–YSZ [37, 119–122], some of which have been successfully used in stainless-steel-supported cells. However, this performance is achieved using high-surface-area nanostructures, the long-term stability of which remains to be demonstrated.

Besides infiltration, another way to introduce nanoparticles is *in situ* by exsolving them from a host oxide. Reduction of certain oxides (such as $La_{0.8}Sr_{0.2}Cr_{0.82}Ru_{0.18}O_{3-\delta}$) by low oxygen partial pressure or cathodic polarization causes reduced metal nanoparticles (such as Ru in that example) to leave the crystal lattice and segregate at the surface [47, 123, 124]. Depending on the materials and exsolution procedure, the nanoparticles can exhibit unique properties—they can be pinned to the surface and thereby be very stable, and oxidation–reduction cycling can make them dissolve into and re-exsolve from the crystal lattice, regenerating their performance. The performance of infiltrated MIEC nanoparticles is also often activated by such oxidation–reduction cycles, the mechanism for which is not yet clear [32, 125, 126].

At present, the only commercially available cells with alternative fuel electrodes than Ni–YSZ use similar composites of Ni and doped ceria, which avoid only some of the issues that plague Ni–YSZ. With further development of advanced nanostructured electrodes with low or no Ni, next-generation cells may be able to integrate them and utilize their advantages.

4 Perspectives and visions for RSOC applications

This section deals briefly with perspectives and visions for RSOC applications with ideas of how to operate RSOC systems, such as systems for providing large sustainable electricity grids based on wind and photoelectric power with short- and long-term (seasonal) storage of energy, and systems for the conversion of power-to-fuel for the transportation sector.

Fig. 27 illustrates how the RSOC potentially can become an essential part of a CO_2 plus H_2O to hydrocarbon recycling system. It is imagined to consist of a device for CO_2 capture from air and a P2F-production unit comprising an SOEC plus a catalytic hydrocarbon synthesis reactor. The latter has been a commercial product using the Fisher-Tropsch process since 1936. In fact, it is today possible to buy (with a long delivery time) all components for such a system. The Swiss company, Climeworks, has commercialized a process for the capture of CO_2 from air and the Danish company, Haldor Topsøe, has commercialized a process called eCOs for the on-site production of CO by electrolysis of CO_2 using SOEC stacks.

We envisage that such systems may be put up in deserts and coupled to photovoltaic or wind turbines (as shown in Fig. 27) in windy areas such as the Danish North Sea or Patagonia in Argentina. Then, products such as CH_4 or DME may be transported in pipelines or tankers to cities that need the fuel. This would have the large advantage that we to a great extent can utilize our existing infrastructure.

Another vision is a large renewable electricity-conversion and storage system using RSOCs. Fig. 28 shows a schematic diagram of such a large-scale storage system using novel, not-yet-realized P2G technology combined with underground gas storage [128, 129].

The novel aspect in this is an RSOC with reversible CH_4 conversion. The already developed P2G technique via syngas described above can in principle be widely deployed but, unfortunately, for long-term, seasonal periods, this technology is expensive and provides a low round-trip efficiency. The high loss of entropy in the H_2O and CO_2 electrolysis (two molecules of H_2O or of CO_2 are converted into three molecules: two H_2 plus one O_2, or two CO plus one O_2). In the case of direct electrochemical synthesis of CH_4 inside the fuel-electrode compartment, the overall reaction is

$$2\,H_2O + CO_2 \rightleftharpoons CH_4 + 2O_2 \qquad (13)$$

There is no change in the number of gas molecules and therefore an almost negligible change in entropy. As mentioned previously, this will require a significant decrease in the RSOC operation temperature to below 500°C combined with an operation pressure of around 30 bar. We think that this may be within reach within a few years if the financial support of the efforts in this area would be just slightly increased. If this target is reached and combined with the sub-surface storage of CO_2 and with CH_4 delivered to or from the natural-gas pipeline network, then this will enable large-scale electricity conversion and storage with a real round-trip efficiency of up to 80% and an estimated storage cost of around 3 US¢ kW^{-1} h^{-1}, i.e. comparable to pumped hydro and much better than previously proposed technologies.

5 Comparison of RSOCs to competing electrochemical-conversion technologies

A comparison of RSOCs to competitive low-temperature (<200°C) electrochemical-conversion technologies is presented in Fig. 29, which shows the ranges of polarization curves for SOECs, PEMECs (polymer electrolyte membrane electrolysis cells) and AECs (alkaline electrolysis cells). Fig. 29 clearly shows that the RSOC has by far the greatest potential to become the most efficient electrolyser. The R&D of RSOCs has improved the durability and reliability a lot since 2011, the year of publication of Fig. 29, so the RSOC is now in early commercialization. There is worldwide

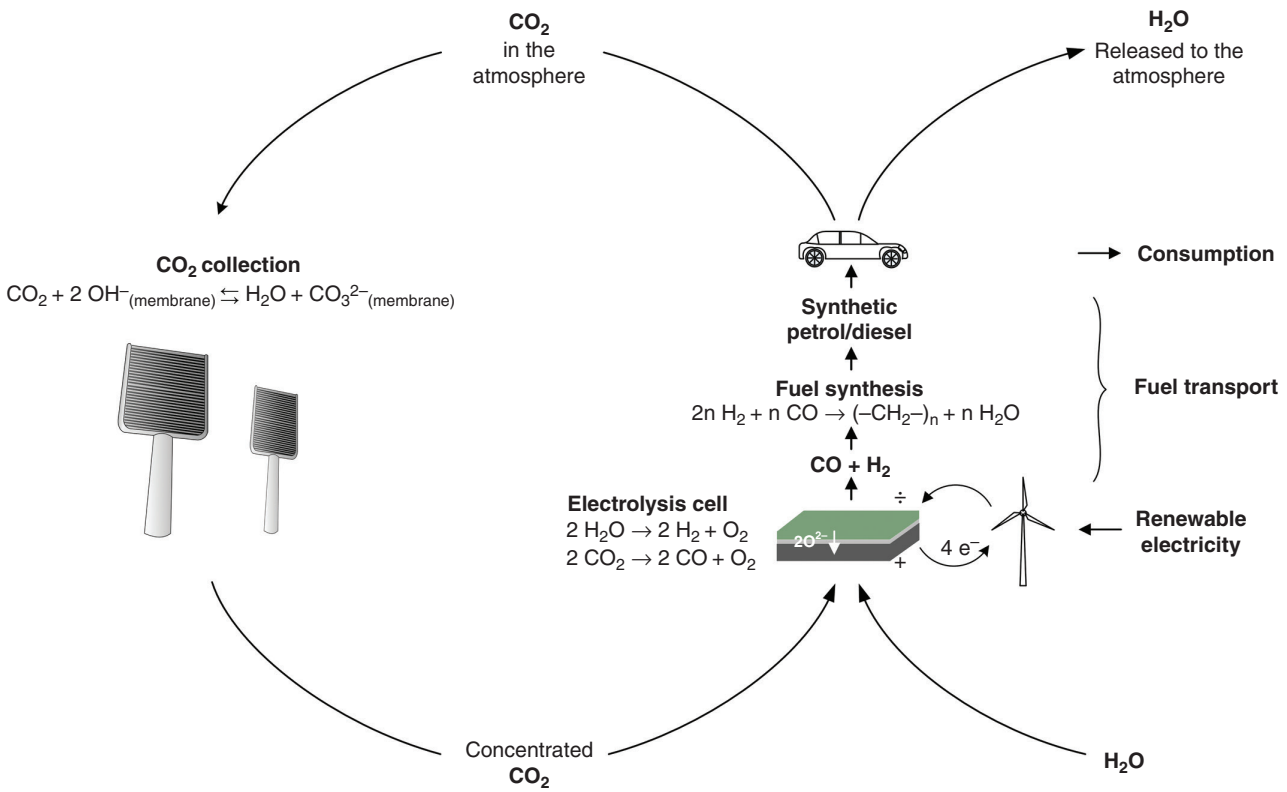

Fig. 27 CO_2 neutral-energy cycle utilizing CO_2 capture from air with the process involving a humidity swing in combination with an SOEC [9, 127]. With permission from American Chemical Society.

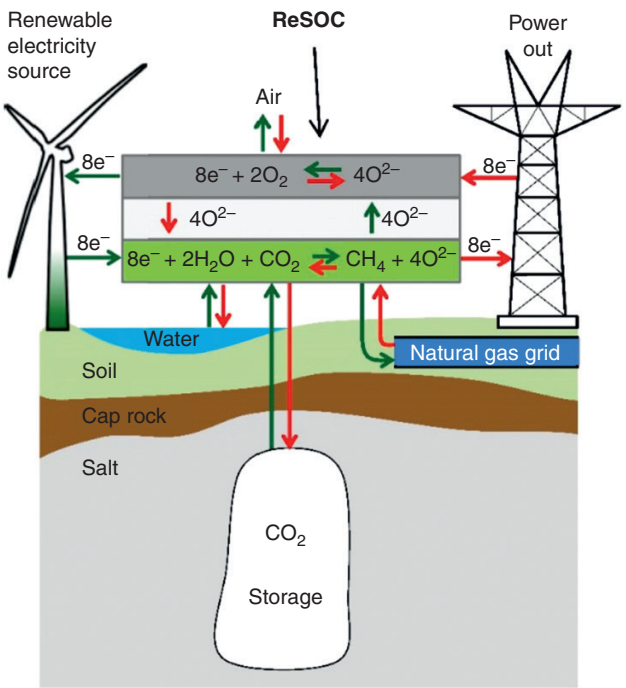

Fig. 28 Schematic diagram of the proposed large-scale electricity-conversion and storage system. When storing renewable electricity (electrolysis mode), the reversible solid-oxide cell (RSOC) converts $CO_2 + H_2O$ into CH_4 (SNG), by extracting oxygen (green lines), and SNG is stored in the natural-gas grid. The process is reversed (red lines) when producing electricity on demand (fuel-cell mode). With permission from Elsevier [129].

increasing R&D activity in the area of all three electrolyser types, so they are all being improved continuously. However, as the low-temperature cells are not reversible, these cell types are competitors only in separate P2F and F2P systems, but not in reversible P2F–F2P systems, as envisaged in Fig. 28.

If a power utility today is going to build a large plant (several 100 MW), it will have to use systems with AECs, as this is the type with the lowest price, and with companies with large production capacity. A drawback of conventional AEC systems is that they are quite voluminous, and therefore the much more compact PEMEC systems, which also are being commercialized these days, are often preferred for demonstration projects. In order to get the RSOC into real commercialization, big investors who will build mass-production factories are needed. The RSOC state of R&D is ready for this and, if the R&D support is kept high, then the short-term prospects of great improvements are assessed to be significantly higher for RSOCs than for AECs and PEMECs. (The principal author of this review is also active in both advanced AECs and in PEMECs).

6 RSOC outlook

Now, we are ready to look at which main R&D undertakings should be carried out in order to promote RSOC commercialization. In the short term, we think that fabrication

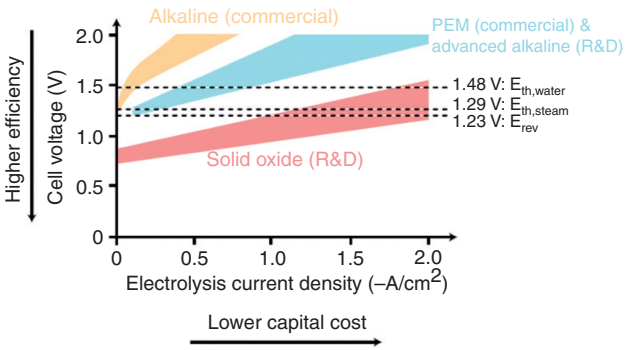

Fig. 29 Typical ranges of polarization curves for different types of state-of-the-art water electrolysis cells. $E_{th,water}$ and $E_{th,steam}$ are the thermoneutral voltages for water and steam electrolysis, respectively. E_{rev} is the reversible potential for water electrolysis at standard state [8]. Reproduced with permission from Elsevier.

methods that can assure a high uniform quality of cells and stacks are most important. As mentioned above, cells with high initial electrochemical performance are also the most durable due to lower electrode overpotential. Furthermore, it is very important to avoid gas leaks through the ~10-μm-thin electrolytes, because, even though leaks through pinholes may not affect the immediate initial cell performance, there will be an increased temperature around the pinhole due to local burning of fuel. This will cause local degradation of both electrodes and electrolyte due to grain and particle coarsening and due to the build-up of local mechanical stresses, which may cause crack formation, and the bad cell will go into an accelerating degradation process that eventually will spread to the adjacent cells.

These efforts may be done using the Ni–YSZ and perovskite-based cells, which are the cells with which we have the most experience. Naturally, all the recent improvements such as ceria additions to Ni–YSZ fuel electrodes, the use of impurity scavengers and the use of the new and stronger zirconia-based Ni cermets for cell support must be implemented. Development of less expensive methods for steam and CO_2-gas cleaning would in particular be helpful.

The next step in cell R&D should be the improvement of new electrodes that are less sensitive to impurities and carbon deposition, and with the more durable metal supports. Preferably, these cells should have operation temperatures below 500°C, as this would decrease the costs of RSOCs for P2F for aeroplanes and other heavy transportation vehicles (Fig. 27) as well as for the conversion and storage of electricity for the grid (Fig. 28).

In parallel to this, it is important to further develop CO_2 air-capture technology, as the cost of CO_2 from air needs to come significantly down in order to make RSOC-based P2F competitive with fossil fuels. In the early phase of commercialization, CO_2 from fossil fuel and biomass power plants and from cement and steel factories may be used.

7 Concluding remarks

The above review supports that the technical and economic problems have been solved to a level at which a next step clearly is large demonstration projects of energy systems. It is also clear that this should be accompanied by a focus on large R&D efforts in the area of energy conversion and storage in general, and that RSOC technology seems particularly attractive for further development, as there are obvious possibilities for significant improvements in an already very promising technology that fits very well into a sustainable-energy system based on solar and wind energy.

P2F is to be preferred over just storing hydrogen, because hydrogen is expensive to handle. Even though the efficiency will be lower for producing fuel, as there is a loss in converting syngas into fuel, it should be noted that we have more than enough inexpensive clean, sustainable energy in the near future and, in general, it is cost and not efficiency that is most important. The efficiency in our consumption of fossil fuel is probably not much above 25% today. The efficiency of the utilization of renewable electricity will most probably become significantly higher—maybe as high as 40%. Thus, all arguments including economics are now in favour of full transition to renewable energy.

Acknowledgements

We acknowledge the financial support from the project 'Maturing SOEC' (Energy Technology Development and Demonstration program, EUDP, project no 64015-0523) and we are grateful to Dr Gurli Mogensen for her great help in discussions and editing this paper.

Conflict of interest

None declared.

References

[1] *Key World Energy Statistics 2018*. http://www.iea.org/statistics/ (3 April 2019, date last accessed).
[2] Tsao J, Lewis N, Crabtree G. *Solar FAQs*. 2006. US Department of Energy. https://www.sandia.gov/~jytsao/Solar%20FAQs.pdf (3 April 2019, date last accessed).
[3] *World Bank Group*. https://globalsolaratlas.info/ (3 April 2019, date last accessed).
[4] IRENA. *Renewable Power Generation Costs in 2017*. Abu Dhabi: International Renewable Energy Agency, 2018, 16. www.irena.org/-/media/Files/IRENA/Agency/Publication/2018/Jan/IRENA_2017_Power_Costs_2018.pdf (2 August 2019, date last accessed).
[5] Vielstich W, Lamm A, Gasteiger HA (eds). *Handbook of Fuel Cells, Fundamentals, Technology and Applications*, Vols. 1–4. New York: John Wiley & Sons Ltd, 2004.
[6] Vielstich W, Yokokawa H, Gasteiger HA (eds). *Handbook of Fuel Cells, Fundamentals, Technology and Applications*, Vols. 5–6. New York: John Wiley & Sons Ltd, 2009.

[7] Kendall K, Kendall M (eds). *High-temperature Solid Oxide Fuel Cells for the 21st Century: Fundamentals, Design and Applications*, 2nd edn. London: Elsevier, 2016.
[8] Graves CR, Ebbesen SD, Mogensen MB, et al. Sustainable hydrocarbon fuels by recycling CO_2 and H_2O with renewable or nuclear energy. *Renew Sust Energ Rev* 2011; 15:1–23.
[9] Ebbesen SD, Jensen SH, Hauch A, et al. High temperature electrolysis in alkaline cells, solid proton conducting cells, and solid oxide cells. *Chem Rev* 2014; 114:10697–734.
[10] Hansen JB. Solid oxide electrolysis—a key enabling technology for sustainable energy scenarios. *Faraday Discuss* 2015; 182:9–48.
[11] Hauch A, Brodersen K, Chen M, et al. Ni/YSZ electrodes structures optimized for increased electrolysis performance and durability. *Solid State Ion* 2016; 293:27–36.
[12] Kilner JA, Druce J, Ishihara T. Electrolytes. In: *High-temperature Solid Oxide Fuel Cells for the 21st Century: Fundamentals, Design and Applications*, 2nd edn. London: Elsevier, 2016, Chapter 4.
[13] Garvie RC, Hannink RHJ, Pascoe RT. Ceramic steel. *Nature* 1975; 258:703–4.
[14] Jiang SP. Development of lanthanum strontium cobalt ferrite perovskite electrodes of solid oxide fuel cells—a review. *Int J Hydrog Energy* 2019; 44:7448–93.
[15] Orera A, Slater PR. New chemical systems for solid oxide fuel cells. *Chem Mater* 2010; 22:675–90.
[16] Xua Z, Lia Y, Wana Y, et al. Nickel enriched Ruddlesden-Popper type lanthanum strontium manganite as electrode for symmetrical solid oxide fuel cell. *J Power Sources* 2019; 425:153–61.
[17] Minh NQ. Cell and stack design, fabrication and performance. In: *High-temperature Solid Oxide Fuel Cells for the 21st Century: Fundamentals, Design and Applications*, 2nd edn, London: Elsevier, 2016, Chapter 8.
[18] Sun X, Chen M, Jensen SH, et al. Thermodynamic analysis of synthetic hydrocarbon fuel production in pressurized solid oxide electrolysis cells. *Int J Hydrog Energy* 2012; 37: 17101–17110.
[19] Jensen SH, Langnickel H, Hintzen N, et al. Pressurized reversible operation of a 30-cell solid oxide cell stack using carbonaceous gases. In: Cigolotti V (ed). *Proceedings of the 7th European Fuel Cell Technology & Applications Conference*. (EFC2017) [EFC17255 EFC17] ENEA 2017, 413–4.
[20] Brown T. *Green Ammonia: Haldor Topsoe's Solid Oxide Electrolyzer*. https://ammoniaindustry.com/haldor-topsoes-solid-oxide-electrolyzer/ (13 April 2019, last day accessed).
[21] Dybkjaer I. Ammonia production process. In: Nielsen A (ed). *Ammonia, Catalysis and Manufacture*. Berlin: Springer-Verlag, 1995, 200–327.
[22] Hagen A. Use of alternative fuels in solid oxide fuel cells. In: *Risø International Energy Conference 2007*, Risø-R-1608(EN), 2007.
[23] US Geological Survey. *Mineral Commodity Summaries 2019: U.S. Geological Survey*, 2019, 116–117. https://doi.org/10.3133/70202434 (14 April 2019, date last accessed).
[24] Brown T. *Ammonia Production Causes 1% of Total Global GHG Emissions. Ammonia Industry*, 26 April 2016. https://ammoniaindustry.com/ammonia-production-causes-1-percent-of-total-global-ghg-emissions/ (14 April 2019, date last accessed).
[25] Wood T, He H, Joia T, et al. Solid oxide electrolysis development at versa power systems. In: *Proceedings of 12th European SOFC & SOE Forum, Chapter 2*, Lucerne, Switzerland, 5–8 July 2016, 183–190.
[26] Borglum B, Ghezel-Ayagh H. Solid Oxide Fuel Cell Development At Versa Power Systems And Fuelcell Energy. In: *Proceedings of 12th European SOFC & SOE Forum, Chapter 2*, Lucerne, Switzerland, 5–8 July 2016, 18–25.
[27] Chen M, Sun X, Hauch A, et al. *Final Report, Project no. 12013 Solid Oxide Electrolysis for Grid Balancing*. https://energiforskning.dk/en/node/7317 (14 April 2019, date last accessed).
[28] Rostrup-Nielsen JR, Hansen JB. Steam reforming for fuel cells. In: *Fuel Cells: Technologies for Fuel Processing*. Oxford, UK: Elsevier, 2011, 49–71.
[29] Hansen JB. Direct reforming fuel cells. In: *Fuel Cells: Technologies for Fuel Processing*. Oxford, UK: Elsevier, 2011, 409–50.
[30] Hansen JB. Fuel processing for fuel cells and power to fuels as seen from an industrial perspective. *J Catalysis* 2015; 328:280–96.
[31] Chen M, Sun X, Chatzichristodoulou C, et al. Thermoneutral operation of solid oxide electrolysis cells in potentiostatic mode. *SOFC-XV, ECS Transactions* 2015; 78:3077–88.
[32] Graves C. Reversing and repairing microstructure degradation in solid oxide cells during operation. *ECS Transactions* 2013; 57:3127.
[33] Skafte TL, Hjelm J, Blennow P, et al. Quantitative review of degradation and lifetime of solid oxide cells and stacks. In: *Proceedings of 12th European SOFC & SOE Forum, Chapter 6*, Lucerne, Switzerland, 5–8 July 2016, 8–27.
[34] Duhn JD, Jensen AD, Wedel S, et al. Optimization of a new flow design for solid oxide cells using computational fluid dynamics modelling. *J Power Sources* 2016; 336:261.
[35] Chen M, Liu YL, Bentzen JJ, et al. Microstructural degradation of Ni/YSZ electrodes in solid oxide electrolysis cells under high current. *J Electrochem Soc* 2013; 160:F883–F891.
[36] Hansen KV, Chen M, Jacobsen T, et al. Effects of strong cathodic polarization of the Ni-YSZ interface. *J Electrochem Soc* 2016; 163:F1217–F1227.
[37] Blennow P, Hjelm J, Klemensø T, et al. Manufacturing and characterization of metal-supported solid oxide fuel cells. *J Power Sources* 2011; 196:7117–25.
[38] Klemensø T, Nielsen J, Blennow P, et al. High performance metal-supported solid oxide fuel cells with Gd-doped ceria barrier layers. *J Power Sources* 2011; 196:9459–66.
[39] Chevalier J, Gremillard L, Virkar AV, et al. The tetragonal-monoclinic transformation in Zirconia: lessons learned and future trends. *J Am Ceram Soc* 2009; 92:1901–20.
[40] Khajavi P. *Improvement of cell strength in high temperature electrolysis cells. Ph.D. Thesis*. Technical University of Denmark, 2018.
[41] Ni DW, Charlas B, Kwok K, et al. Influence of temperature and atmosphere on the strength and elastic modulus of solid oxide fuel cell anode supports. *J Power Sources* 2016; 311:1–12.
[42] Goutianos S, Frandsen HL, Sørensen BF. Fracture properties of nickel-based anodes for solid oxide fuel cells. *J Eur Ceram Soc* 2010; 30:3173–9.
[43] Fleischhauer F, Bermejo R, Danzer R, et al. High temperature mechanical properties of zirconia tapes used for electrolyte supported solid oxide fuel cells. *J Power Sources* 2015; 273:237–43.
[44] Boccaccini N, Frandsen HL, Soprani S, et al. Influence of porosity on mechanical properties of tetragonal stabilized zirconia. *J Eur Ceram Soc* 2018; 38:1720–35.
[45] Frandsen HL, Makowska M, Chatzichristodoulou C, et al. Accelerated creep in solid oxide fuel cell anode supports during reduction. *J Power Sources* 2016; 323:78–89.
[46] Njodzefon JC, Graves CR, Mogensen MB, et al. Kinetic studies on state of the art solid oxide cells: A comparison between hydrogen/steam and reformate fuels. *J Electrochem Soc* 2016; 163:F1451–F1462.
[47] Irvine JTS, Neagu D, Verbraeken MC, et al. Evolution of the electrochemical interface in high-temperature fuel cells and electrolysers. *Nat Energy* 2016; 1:15014.

[48] Knibbe R, Traulsen ML, Hauch A, et al. Solid oxide electrolysis cells: degradation at high current densities. *J Electrochem Soc* 2010; 157:B1209.

[49] Ebbesen S, unpublished DTU results.

[50] Mogensen MB, Hauch A, Sun X, et al. Relation between Ni particle shape change and Ni migration in Ni–YSZ electrodes – a hypothesis. *Fuel Cells* 2017; 17:434–441.

[51] Tao Y, Ebbesen SD, Mogensen MB. Degradation of solid oxide cells during co-electrolysis of steam and carbon dioxide at high current densities. *J Power Sources* 2016; 328:452–462.

[52] Liu Y, Sun X, Bowen JR, et al. Quantification of Ni depletion in long-term tested solid oxide electrolysis cells. Unpublished work.

[53] Jensen SH, Hauch A, Sun X, et al. Coupling Ni migration to gas concentration gradients and reaction site heating. Unpublished work.

[54] Chatzichristodoulou C, Chen M, Hendriksen PV, et al. Understanding degradation of solid oxide electrolysis cells through modeling of electrochemical potential profiles. *Electrochim Acta* 2016; 189:265–82.

[55] Hagen A, Barfod R, Hendriksen PV, et al. Degradation of anode supported SOFCs as a function of temperature and current load. *J Electrochem Soc* 2006; 153:A1165–71.

[56] Ovtar S, Tong X, Bentzen JJ, et al. Boosting the performance and durability of Ni/YSZ cathode for hydrogen production at high current densities via decoration with nano-sized electrocatalysts. *Nanoscale* 2019; 11:4394–406.

[57] Ahlgren E, Poulsen FW. Thermoelectric power of YSZ. *Solid State Ion* 1994; 70:528–32.

[58] Küngas R. Personal communication about Ni migration in cathodically polarized Ni/YSZ electrodes with CO_2/CO. 2018.

[59] Toudahl KK. *Investigation of Electrode Microstructure Degradation in Solid Oxide Electrolysis Stacks*. Project Report, Lyngby, DK: Technical University of Denmark, 2017.

[60] Gubner A, Landes H, Metzger J, et al. Investigations into the degradation of the cermet anode of a solid oxide fuel cell. *ECS Proceedings Volumes* 1997; 40:844–50.

[61] Bao J, Krishnan GN, Jayaweera P, et al. Effect of various coal contaminants on the performance of solid oxide fuel cells: part II: ppm and sub-ppm level testing. *J Power Sources* 2009; 193:617–24.

[62] Graves C, Ebbesen SD, Jensen SH, et al. Eliminating degradation in solid oxide electrochemical cells by reversible operation. *Nat Mater* 2015; 14:239–244.

[63] Huang K, Goodenough JB. *Solid Oxide Fuel Cell Technology*. Oxford: Woodhead Publishing Ltd, 2009.

[64] Boldrin P, Ruiz-Trejo E, Mermelstein J, et al. Strategies for carbon and sulfur tolerant solid oxide fuel cell materials, incorporating lessons from heterogeneous catalysis. *Chem Rev* 2016; 116:13633–84.

[65] Mogensen M, Hansen KV. Impact of impurities and interface reaction on electrochemical activity. In: Vielstich W, Yokokawa H, Gasteiger HA (eds). *Handbook of Fuel Cells*, Vol. 5. New York: John Wiley & Sons Ltd, 2009, 543–54.

[66] Hauch A, Jensen SH, Bilde-Sørensen JB, et al. Silica segregation in the Ni/YSZ electrode. *J Electrochem Soc* 2007; 154:A619–26.

[67] Hauch A, Bowen JR, Kuhn LT, et al. Nanoscale chemical analysis and imaging of solid oxide cells. *Electrochem Solid-State Lett* 2008; 11:B38–41.

[68] Liu YL, Primdahl S, Mogensen M. Effects of impurities on microstructure in the Ni/YSZ–YSZ interface in solid oxide fuel cells. *Solid State Ion* 2003; 161:1–10.

[69] Hansen JB, Rostrup-Nielsen J. Sulfur poisoning on Ni catalyst and anodes. In: Vielstich W, Yokokawa H, Gasteiger HA (eds). *Handbook of Fuel Cells, Fundamentals, Technology and Applications*, Vol. 5–6. New York: John Wiley & Sons Ltd, 2009, Chapter 65.

[70] Hansen JB. Correlating sulfur poisoning of SOFC nickel anodes by a Temkin isotherm. *Electrochem Solid-State Let* 2008; 11:B178–80.

[71] Ebbesen SD, Mogensen M. Exceptional durability of solid oxide cells. *Electrochem Solid-State Lett* 2010; 13:B106–8.

[72] Hauch A, Hagen A, Hjelm J, et al. Sulfur poisoning of Ni/stabilized-zirconia anodes—effect on long-term durability. *ECS Transactions* 2013; 57:615–25.

[73] Yin X, Bencze L, Motalov V, et al. Thermodynamic perspective of Sr-related degradation issues in SOFCs. *Int J Appl Ceram Technol* 2018; 15:380–90.

[74] Horita T, Cho DH, Wang F, et al. Degradation mechanism of SOFC cathodes under CrO_3 and SO_2 impurity exposures. *ECS Transactions* 2013; 51:69–77.

[75] Hilpert K, Dos D, Miller M, et al. Chromium vapor species over solid oxide fuel cell interconnect materials and their potential for degradation processes. *J Electrochem Soc* 1996; 143:3642–3.

[76] Mah JCW, Muchtar A, Somalu MR, et al. Metallic interconnects for solid oxide fuel cell: a review on protective coating and deposition techniques. *Int J Hydrog Energy* 2017; 42:9219–29.

[77] Helveg S, Sehested J, Rostrup-Nielsen JR. Whisker carbon in perspective. *Catal Today* 2011; 178:42–6.

[78] Helveg S, López-Cartes C, Sehested J, et al. Atomic-scale imaging of carbon nanofibre growth. *Nature* 2004; 427:426–9.

[79] Gohier A, Ewels CP, Minea TM, et al. Carbon nanotube growth mechanism switches from tip- to base-growth with decreasing catalyst particle size. *Carbon N Y* 2008; 46:1331–8.

[80] Rao R, Sharma R, Abild-Pedersen F, et al. Insights into carbon nanotube nucleation: cap formation governed by catalyst interfacial step flow. *Sci Rep* 2014; 4:6510.

[81] Tao Y, Ebbesen SD, Zhang W, et al. Carbon nanotube growth on nanozirconia under strong cathodic polarization in steam and carbon dioxide. *ChemCatChem* 2014; 4000:1220–4.

[82] Tao Y, Ebbesen SD, Mogensen MB. Carbon deposition in solid oxide cells during co-electrolysis of H_2O and CO_2. *J Electrochem Soc* 2014; 161:F337–43.

[83] Skafte TL, Blennow P, Hjelm J, et al. Carbon deposition and sulfur poisoning during CO_2 electrolysis in nickel-based solid oxide cell electrodes. *J Power Sources* 2018; 373:54–60.

[84] Duboviks V, Maher RC, Kishimoto M, et al. Raman spectroscopic study of the carbon deposition mechanism on Ni/CGO electrodes during CO/CO_2 electrolysis. *Phys Chem Chem Phys* 2014; 16:13063.

[85] Hauch A, Skafte TL, Küngas R, et al. CO_2 electrolysis—how gas purity and over-potential affect detrimental carbon deposition. In: *Proceedings 13th European SOFC & SOE Forum*, Lucerne, Switzerland, 3–6 July 2018, B1501.

[86] Navasa M, Frandsen HL, Skafte TL, et al. Localized carbon deposition in solid oxide electrolysis cells studied by multiphysics modeling. *J Power Sources* 2018; 394:102–13.

[87] Duhn JD, Jensen AD, Wedel S, et al. Modeling of gas diffusion in Ni/YSZ electrodes in CO_2 and co-electrolysis. *Fuel Cells* 2017; 2017:442–56.

[88] Duboviks V, Lomberg VM, Maher RC, et al. Carbon deposition behaviour in metal-infiltrated gadolinia doped ceria electrodes for simulated biogas upgrading in solid oxide electrolysis cells. *J Power Sources* 2015; 293:912–21.

[89] Maher RC, Duboviks V, Offer GJ, et al. Raman spectroscopy of solid oxide fuel cells: technique overview and application to carbon deposition analysis. *Fuel Cells* 2013; 13:455–69.

[90] Murray EP, Tsai T, Barnett SA. A direct-methane fuel cell with a ceria-based anode. *Nature* 1999; 400:649–51.

[91] Park S, Vohs JM, Gorte RJ. Direct oxidation of hydrocarbons in a solid-oxide fuel cell. *Nature* 2000; 404:265–7.
[92] Skafte TL, Hjelm J, Blennow P, et al. Reactivating the Ni-YSZ electrode in solid oxide cells and stacks by infiltration. *J Power Sources* 2018; 378:685–90.
[93] Lee JG, Jeon OS, Hwang HJ, et al. Durable and high-performance direct-methane fuel cells with coke-tolerant ceria-coated Ni catalysts at reduced temperatures. *Electrochim Acta* 2016; 191:677–86.
[94] Skafte TL, Guan Z, Machala ML, et al. *Selective High-temperature CO_2 Electrolysis Enabled by Oxidized Carbon Intermediates*. accepted for publication in Nature Energy, 2019.
[95] Gross MD, Vohs JM, Gorte RJ. Recent progress in SOFC anodes for direct utilization of hydrocarbons. *J Mater Chem* 2007; 17:3071.
[96] Wu X, Tian Y, Zhang J, et al. Enhanced electrochemical performance and carbon anti-coking ability of solid oxide fuel cells with silver modified nickel-yttrium stabilized zirconia anode by electroless plating. *J Power Sources* 2016; 301:143–50.
[97] Rostrup-Nielsen JR. Sulfur-passivated nickel catalysts for carbon-free steam reforming of methane. *J Catal* 1984; 85:31–43.
[98] Neagu D, Oh T-S, Miller DN, et al. Nano-socketed nickel particles with enhanced coking resistance grown in situ by redox exsolution. *Nat Commun* 2015; 6:8120.
[99] Subotic V, Schluckner C, Stöckl B, et al. Strategy for carbon gasification from porous Ni-YSZ anodes of industrial-sized ASC-SOFCs and effects of carbon growth. *J Electrochem Soc* 2016; 163:F1515–22.
[100] Njodzefon JC, Graves CR, Mogensen MB, et al. Kinetic studies on state of the art solid oxide cells: a comparison between hydrogen/steam and reformate fuels. *J Electrochem Soc* 2016; 163:F1451–62.
[101] Leonide A, Apel Y, Ivers-Tiffée E. SOFC modeling and parameter identification by means of impedance spectroscopy. *ECS Transactions* 2009; 19:81–109.
[102] Samson AJ, Hjalmarsson P, Søgaard M, et al. Highly durable anode supported solid oxide fuel cell with an infiltrated cathode. *J Power Sources* 2012; 216:124–30.
[103] Graves C, Martinez L, Sudireddy BR. High performance nanoceria electrodes for solid oxide cells. *ECS Transactions* 2016; 72:183–92.
[104] Metcalfe IS, Middleton PH, Petrolekas P, et al. Hydrocarbon activation in solidstate electrochemical cells. *Solid State Ion* 1992; 57:259–64.
[105] Mogensen M, Lindegaard T, Hansen UR, et al. Physical properties of mixed conductor solid oxide fuel cell anodes of doped CeO_2. *J Electrochem Soc* 1994; 141:2122–8.
[106] Tao S, Irvine JTS. A redox-stable efficient anode for solid oxide fuel cells. *Nat Mater* 2003; 2:320–3.
[107] Tao S, Irvine JTS. Catalytic properties of the perovskite oxide $La_{075}Sr_{025}Cr_{05}Fe_{05}O_{3-\delta}$ in relation to its potential as a solid oxide fuel cell anode material. *Chem Mater* 2004; 16:4116–21.
[108] Haag JM, Madsen BD, Barnett SA, et al. Application of $LaSr_2Fe_2CrO_{9-\delta}$ in solid oxide fuel cell anodes. *Electrochem Solid-State Lett* 2008; 11:B51–3.
[109] Chen M, Paulson S, Thangadurai V, et al. Sr-rich chromium ferrites as symmetrical solid oxide fuel cell electrodes. *J Power Sources* 2013; 236:68–79.
[110] Huang Y-H, Dass RI, Xing Z-L, et al. Double perovskites as anode materials for solid-oxide fuel cells. *Science* 2006; 312:254–7.
[111] Huang Y-H, Liang G, Croft M, et al. Double-perovskite anode materials Sr_2MMoO_6 (M = Co, Ni) for solid oxide fuel cells. *Chem Mater* 2009; 21:2319–26.
[112] Graves C, Sudireddy BR, Mogensen M. Molybdate based ceramic negative-electrode materials for solid oxide cells. *ECS Transactions* 2010; 28:173–92.
[113] Liu Q, Dong X, Xiao G, et al. A novel electrode material for symmetrical SOFCs. *Adv Mater* 2010; 22:5478–82.
[114] Osinkin DA, Lobachevskaya NI, Suntsov AY. The electrochemical behavior of the promising $Sr_2Fe_{15}Mo_{05}O_{6-\delta}$ + $Ce_{08}Sm0_2O_{19-\delta}$ anode for the intermediate temperature solid oxide fuel cells. *J Alloys Compd* 2017; 708:451–5.
[115] Sengodan S, Choi S, Jun A, et al. Layered oxygen-deficient double perovskite as an efficient and stable anode for direct hydrocarbon solid oxide fuel cells. *Nat Mater* 2015; 14:205–9.
[116] Choi S, Sengodan S, Park S, et al. A robust symmetrical electrode with layered perovskite structure for direct hydrocarbon solid oxide fuel cells: $PrBa_{08}Ca_{02}Mn_2O_{5+\delta}$. *J Mater Chem A* 2016; 4:1747–53.
[117] Marina OA, Pederson LR, Williams MC, et al. Electrode performance in reversible solid oxide fuel cells. *J Electrochem Soc* 2007; 154:B452–9.
[118] Craciun R, Park S, Gorte RJ, et al. A novel method for preparing anode cermets for solid oxide fuel cells. *J Electrochem Soc* 1999; 146:4019–22.
[119] Tucker MC, Lau GY, Jacobson CP, et al. Stability and robustness of metal-supported SOFCs. *J Power Sources* 2008; 175:447–51.
[120] Zhan Z, Bierschenk DM, Cronin JS, et al. A reduced temperature solid oxide fuel cell with nanostructured anodes. *Energy Environ Sci* 2011; 4:3951–4.
[121] Skafte TL, Sudireddy BR, Blennow P, et al. Carbon and redox tolerant infiltrated oxide fuel-electrodes for solid oxide cells. *ECS Transactions* 2016; 72:201–14.
[122] Dogdibegovic E, Wang R, Lau GY, et al. High performance metal-supported solid oxide fuel cells with infiltrated electrodes. *J Power Sources* 2019; 410–411:91–8.
[123] Madsen BD, Kobsiriphat W, Wang Y, et al. Nucleation of nanometer-scale electrocatalyst particles in solid oxide fuel cell anodes. *J Power Sources* 2007; 166:64–7.
[124] Kwon O, Kim K, Joo S, et al. Self-assembled alloy nanoparticles in a layered double perovskite as a fuel oxidation catalyst for solid oxide fuel cells. *J Mater Chem A* 2018; 6:15947–53.
[125] Blennow P, Hansen KK, Wallenberg LR, et al. Synthesis of Nb-doped $SrTiO_3$ by a modified glycine-nitrate process. *J Eur Ceram Soc* 2007; 27:3609–12.
[126] Corre G, Kim G, Cassidy M, et al. Activation and ripening of impregnated manganese containing perovskite SOFC electrodes under redox cycling. *Chem Mater* 2009; 21:1077–84.
[127] Lackner KS. Capture of carbon dioxide from ambient air. *Eur Phys J Special Topics* 2009; 176:93–106.
[128] Jensen SH, Graves CR, Mogensen M, et al. Large-scale electricity storage utilizing reversible solid oxide cells combined with underground storage of CO_2 and CH_4. *Energy Environ Sci* 2015; 8:2471–9.
[129] Butera G, Jensen SH, Clausen LR. A novel system for large-scale storage of electricity as synthetic natural gas using reversible pressurized solid oxide cells. *Energy* 2019; 166:738–54.